State estimation and advanced control of the 2D temperature field in an experimental oscillating annealing device

authored by **L. Jadachowski, A. Steinboeck, and A. Kugi**

and published in *Control Engineering Practice*.

Contact:

Automation and Control Institute (ACIN)
Vienna University of Technology
Gusshausstrasse 27-29/E376
1040 Vienna, Austria

Internet: www.acin.tuwien.ac.at
E-mail: office@acin.tuwien.ac.at
Phone: +43 1 58801 37601
Fax: +43 1 58801 37699

State estimation and advanced control of the 2D temperature field in an experimental oscillating annealing device

L. Jadachowski[a,*], A. Steinböck[b], A. Kugi[a]

[a] *Christian Doppler Laboratory for Model-Based Control in the Steel Industry, Automation and Control Institute, Vienna University of Technology, Gußhausstraße 27-29, 1040 Vienna, Austria*
[b] *Automation and Control Institute, Vienna University of Technology, Gußhausstraße 27-29, 1040 Vienna, Austria*

Abstract

Annealing plays a crucial role in industrial steel strip production lines. Laboratory annealing devices are experimental furnaces that allow the simulation of the annealing process in large-scale production lines and are employed, e.g., to design new or improve existing heat treatment cycles. The furnace considered in this paper is equipped with individually controlled infrared heaters. It is used to reheat flat specimens of steel strips accurately and homogeneously in space according to predefined temperature trajectories. In view of the complex furnace geometry with highly specular surfaces and thermal radiation as the main heat transfer mode, the operation of this furnace constitutes a 2-dimensional nonlinear distributed-parameter thermal control problem. The basic control inputs are the electric powers of infrared heating lamps, which are controlled by six phase-fired thyristors. For temperature tracking, a two-degree-of-freedom control concept is applied, which comprises an optimal feedforward controller and a state feedback controller. The feedforward controller is based on the solution of a dynamic optimization problem. The feedback part contains a Linear-Quadratic-Gaussian controller, which requires knowledge of the actual temperature field of the specimen. Since in the considered annealing device, this temperature field cannot be completely measured, an extended Kalman filter is used for the estimation of spatial temperature profiles. This estimation is based on just three local measurements of the surface temperature of the specimen. The proposed control approach was implemented and experimentally validated in several annealing runs. The effect of an oscillating motion of the specimen on the temperature homogeneity is investigated by comparisons of measurement results with a fixed specimen position. It is shown that the temperature inhomogeneity can be significantly reduced if the specimen oscillation is systematically taken into account in the mathematical model, the state estimation, and the control design.

Keywords: Non-local quasilinear parabolic PDE, Model averaging, Model reduction, Temperature field control, Optimal feedforward control, Extended Kalman filtering, Linear-Quadratic-Gaussian feedback control

1. Introduction

In the steel industry, annealing is a heat treatment process to reduce internal stresses, to ensure specific metallurgical properties, or to prepare optimum surface conditions for subsequent production operations, e.g., hot-dip galvanization (Totten, 2006; Bordignon et al., 2002). Annealing is a typical processing step in strip production lines, where the temperature evolution of the strip should follow a desired reference trajectory.

So called continuous-type annealing furnaces are used in the steel industry for heat treatment of strips in production lines (Mullinger and Jenkins, 2014). The coiled strip is uncoiled and conveyed with a velocity in the range of 1.5–3 m/s through the furnace and the temperature evolution along the length of the axially moving strip, i.e., along one spatial variable, has to be controlled according to the metallurgical requirements, see, e.g., (Strommer et al., 2018; Niederer et al., 2016).

Batch-operated annealing devices are typically employed for laboratory reasons. In the steel industry, they serve as experimental ovens to develop and investigate new annealing curves, to emulate continuous production lines, and to optimize their process parameters. Seyrkammer et al. (2010) developed a tracking controller for the mean temperature of a sheet metal specimen in a laboratory annealing test rig with Ohmic heating. Depending on the furnace design and the heating elements, other laboratory-scale furnaces allow also to control the spatial temperature distribution in the specimens. This is especially true for the experimental furnace considered in this paper. The furnace is operated by voestalpine Stahl GmbH to simulate and improve continuous annealing processes in the production lines. In the considered experimental furnace, flat specimens are heated by electrically powered infrared (IR) lamps. They are connected and controlled in groups to minimize temperature inhomogeneities

*Corresponding author. Tel.: +43 1 58801-376266 Email address: jadachowski@acin.tuwien.ac.at (L. Jadachowski)

Post-print version of the article: L. Jadachowski, A. Steinboeck, and A. Kugi, "State estimation and advanced control of the 2D temperature field in an experimental oscillating annealing device", *Control Engineering Practice*, vol. 78, pp. 116–128, 2018, ISSN: 0967-0661. DOI: 10.1016/j.conengprac.2018.06.011

of the specimen. Such inhomogeneities can be caused by an inadequate temperature controller that does not take into account the distributed nature of the system. Moreover, they may result from electric power limitations combined with a fixed and unsuitable geometric arrangement of the IR-lamps and the specimen. Hence, accurate control of 2-dimensional (2D) temperature fields plays an important role when operating such annealing devices.

A thorough review of the relevant literature reveals only few papers that consider practical implementation and experimental validation of 2D temperature control. A combination of the flatness-based feedforward controller and proportional-integral-derivative output error feedback controller is proposed by Böhm and Meurer (2017) to control the temperature evolution of a deep drawing tool at 12 sensor positions. Girault and Videcoq (2013) considered an experimental device with a thin aluminum plate heated by a mobile radiative heat source. They employ a Linear-Quadratic Regulator to control the temperature of the plate at 3 locations around the steady-state temperature distribution. They use a Kalman filter with up to 8 thermocouple measurements for temperature estimation. Control of the temperature homogeneity is also a traditional research topic in semiconductor manufacturing. In (Logerais et al., 2015; Ebert et al., 2004), the authors mainly focus on the temperature profiles along the radial coordinate of the rotating circular wafers while assuming homogeneity along the tangential direction. Temperature control along a single spatial variable is also addressed by Abeykoon et al. (2011) and Lipár et al. (2013) in polymer extrusion processes and by Shen et al. (2016) in aluminum quenching furnaces.

The main contribution of this paper is the development and implementation of an advanced control concept for the 2D temperature field of the specimen in an oscillating annealing furnace. The proposed control approach consists of an optimal feedforward controller, a state observer for the 2D temperature profile, and a state feedback control law with an integral term. The main goal is to determine trajectories of the electric power supplied to the IR-lamps to ensure that the real temperature field of the specimen follows a desired reference temperature. In particular, the primary control objective is that the mean specimen temperature tracks the desired trajectory $T_{\mathrm{ref}}(t)$, which defines a transition of the mean temperature between two steady-state values within a finite time t_E. A simultaneous minimization of the temperature inhomogeneity constitutes the secondary control objective. Under nominal furnace conditions, both control objectives are satisfied by the model-based feedforward controller developed by Jadachowski et al. (2018). The underlying mathematical model was presented by Jadachowski et al. (2017b) for a fixed specimen position and extended in (Jadachowski et al., 2018) to capture also the oscillating motion of the specimen. To allow for the compensation of tracking errors, a Linear-Quadratic-Gaussian (LQG) feedback controller is designed. It requires the estimation of time evolutions of 2D temperature fields of the specimen. For this, an extended Kalman filter (EKF) is developed on the basis of the specimen temperature model and three local measurements of the specimen surface temperature. The overall estimation and control performance is evaluated by measurements. Different annealing cycles were performed to investigate the accuracy of the temperature estimation and the tracking controller and to examine the effect of the oscillating motion on the temperature homogeneity of the specimen.

The paper is structured as follows: In Section 2, the development of three mathematical models of the temperature evolution in the oscillating specimen is summarized. This includes a full-state finite-difference model, a reduced-order finite-element model, and a reduced-order time-averaged model. In Section 3, the temperature estimation problem is formulated and the EKF is designed. Section 4 is dedicated to the tracking control strategy consisting of the optimal feedforward controller and the LQG feedback law with the integral control action. Measurement and estimation results are presented and analyzed in Section 5. Final remarks are given in Section 6.

Notation: Arguments of functions are omitted whenever they are clear from the context. Moreover, $\nabla T(\mathbf{x},t)$ denotes the temperature gradient with respect to the spatial coordinates $\mathbf{x}=(x,y)$, and $\partial_* T(\mathbf{x},t)$ denotes the partial derivative w.r.t. $*$. Temperatures of the entity $\star$ are assembled in the vector $\mathbf{T}_\star = \left[T_{\star,i}\right]$. The vector of their fourth powers is written in the form $\mathbf{T}_\star^4 = \left[T_{\star,i}^4\right]$. Finally, $\mathbf{1}_n$ refers to the vector of dimension n with all entries equal to 1 and $\mathbf{I}$ is the identity matrix.

2. Mathematical modeling

The geometry of the considered furnace is presented in Fig. 1. It shows cross-sections of the heating chamber. This chamber consists of a water-cooled housing with a flat steel specimen (length L_s, width W_s, thickness B_s) clamped between two specimen holders, which can be moved vertically. On both sides of the specimen, two arrays of IR-lamps (N_h horizontal and N_v vertical IR-lamps) are mounted on gold-coated water-cooled reflectors. The distance between two horizontal and two vertical lamps is L_h and L_v, respectively. Inert gas streams into the heating zone through a gap between the upper specimen holder and the housing and leaves the IR-zone via the bottom gap. When supplying electric power to the IR-lamps, the specimen is heated by means of thermal radiation. In particular, the spatial temperature field in the specimen fillet $\Omega_f := \{(x,y)\in\mathbb{R}^2 \mid 0.25L_s < x < 0.75L_s,\ 0.2W_s < y < 0.8W_s\}$, with the area $A_f = L_f W_f$ and the dimensions $L_f = 0.5L_s$ and $W_f = 0.6W_s$, is of main interest. A small Biot-number $Bi \approx 8.87\times10^{-4} \ll 1$ (cf. Incropera et al., 2007) justifies the assumption of a homogeneous strip temperature along the thickness direction z. The IR-lamps are controlled in groups by means of six phase-fired thyristors.

Post-print version of the article: L. Jadachowski, A. Steinboeck, and A. Kugi, "State estimation and advanced control of the 2D temperature field in an experimental oscillating annealing device", *Control Engineering Practice*, vol. 78, pp. 116–128, 2018, ISSN: 0967-0661. DOI: 10.1016/j.conengprac.2018.06.011

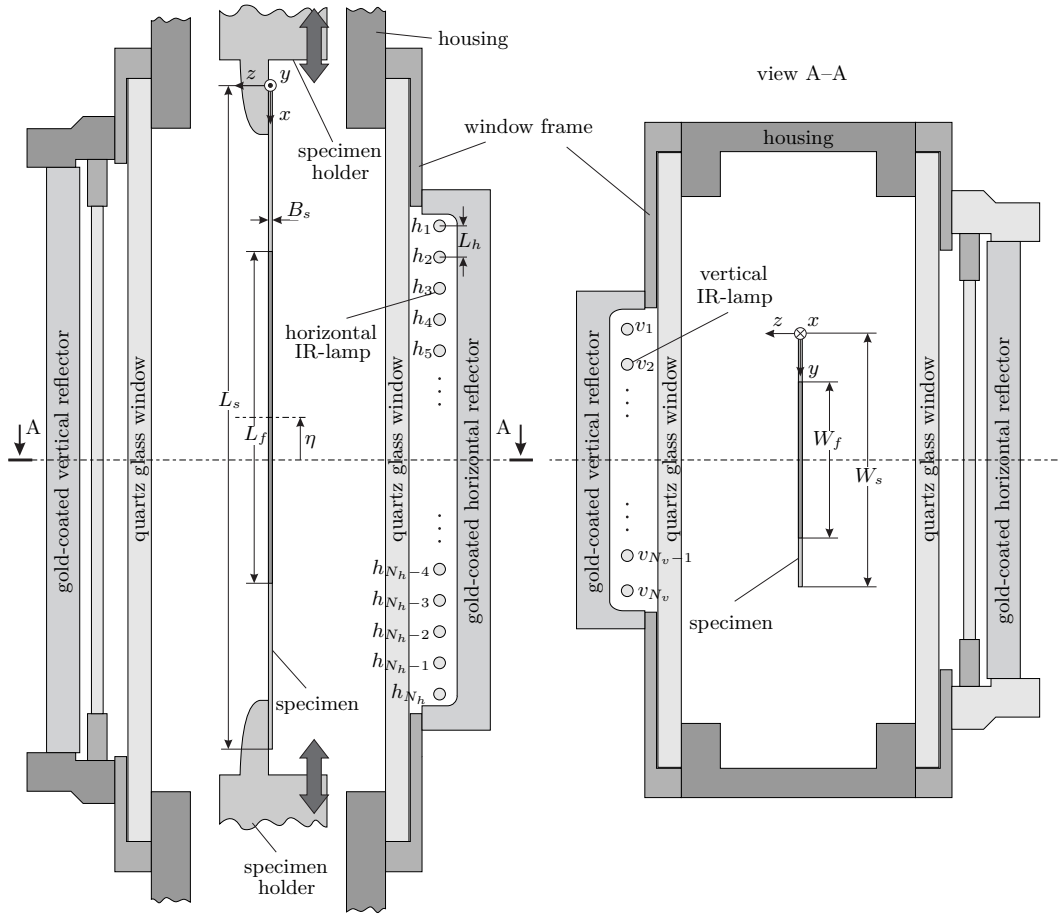

Figure 1: Cross-sectional views of the experimental annealing furnace: (left) view from the side, (right) view from the top. Two-sided arrow indicates an oscillating motion of the specimen and the specimen holders with respect to the IR-lamps and furnace walls. For $\eta = 0$ the specimen is in the center of the heating chamber of the furnace.

Four thyristors T_i^h, $i = 1, \ldots, 4$ are used for the horizontal lamps and two T_i^v, $i = 1, 2$ for the vertical lamps. The mobile specimen holders allow the specimen to oscillate vertically with a maximum amplitude of $\bar{\eta} = 0.25 L_f$.

In the following, three mathematical models of the temperature evolution in the oscillating specimen are briefly summarized for reference. The presentation of a full-order finite-difference (FD) model is followed by a reduced-order finite-element (FE) model. The third model is obtained by time averaging of the FE model.

2.1. Full-order FD-model of an oscillating specimen

A distributed-parameter first principles model of the 2D spatio-temporal temperature evolution for a non-moving steel specimen was derived and validated by Jadachowski et al. (2017b). In (Jadachowski et al., 2018), this temperature model was extended to take into account the oscillating motion of the specimen. The specimen position $\eta(t)$ varies periodically in time along the vertical direction whereas the IR-lamps have fixed positions. In view of this motion, the Lagrangian coordinates xyz are used, i.e., the frame $(0xyz)$ is fixed to the specimen. The model describes the 2D temperature field $T(\mathbf{x}, t)$ of the specimen in K by the time-varying quasilinear non-local parabolic PDE

$$\rho c_p(T) \partial_t T(\mathbf{x}, t) = \nabla \cdot \big(\lambda(T) \nabla T(\mathbf{x}, t)\big) + \dot{q}(\mathbf{x}, T, \mathbf{u}, \eta), \quad (1)$$

which depends on the time t and the spatial coordinates $\mathbf{x} = (x, y) \in \Omega := \{\mathbf{x} \in \mathbb{R}^2 \mid 0 < x < L_s,\ 0 < y < W_s\}$. Moreover, ρ in $\mathrm{kg/m^3}$ denotes the mass density, $c_p(T)$ in $\mathrm{J/(kg\,K)}$ the specific heat capacity, and $\lambda(T)$ in $\mathrm{W/(m\,K)}$ the thermal conductivity. In (2), the source term

$$\dot{q}(\mathbf{x}, T, \mathbf{u}, \eta) = -\frac{\dot{q}_r(\mathbf{x}, T, \mathbf{u}, \eta) + \dot{q}_c(\mathbf{x}, T) + \dot{q}_h(\mathbf{x}, T)}{B_s} \quad (2)$$

Post-print version of the article: L. Jadachowski, A. Steinboeck, and A. Kugi, "State estimation and advanced control of the 2D temperature field in an experimental oscillating annealing device", *Control Engineering Practice*, vol. 78, pp. 116–128, 2018, ISSN: 0967-0661. DOI: 10.1016/j.conengprac.2018.06.011

contains the net heat flux (W/m^2) due to thermal radiation $\dot{q}_r(\mathbf{x}, T, \mathbf{u}, \eta)$, forced convection $\dot{q}_c(\mathbf{x}, T)$, and heat losses into the specimen holders $\dot{q}_h(\mathbf{x}, T)$. Note that the specimen motion is captured only by $\dot{q}_r(\mathbf{x}, T, \mathbf{u}, \eta)$, while the latter heat transfer mechanisms are assumed to be independent of $\eta(t)$. The control inputs $\mathbf{u}^{\mathrm{T}}(t) = \begin{bmatrix}\mathbf{u}_h^{\mathrm{T}}(t) & \mathbf{u}_v^{\mathrm{T}}(t)\end{bmatrix}$ define the net radiative power emitted by the horizontal and vertical IR-lamps with $\mathbf{u}_\star(t) = [u_{\star,i}(t)]_{i=1,\dots,N_\star}$, $\star \in \{h, v\}$. In fact, $u_{\star,i}(t) = p^\star_{el,i}(t)/(\pi d_\star l_\star)$ in W/m^2 is the net heat flux density at the surface of lamp i, which has the effective diameter $d_\star$ and the length $l_\star$. Given the typically high temperatures in the furnace, it is assumed that the entire electric power $p^\star_{el,i}(t)$ supplied to the lamp i is converted into thermal radiation. The control variables are box-constrained, i.e., $\mathbf{0} \le \mathbf{u}(t) \le \bar{u}\mathbf{1}_{N_v+N_h}$ with the maximum lamp power $\bar{u}$.

The boundary conditions are postulated to be independent of $\eta(t)$ and defined on $\mathbf{x} \in \Gamma := \mathrm{cl}(\Omega) \setminus \Omega$ by

$$\lambda(T)\partial_x T(\mathbf{x}, t) = \alpha_h \left(T(\mathbf{x}, t) - T_h^{up}\right), \qquad x = 0 \tag{3a}$$
$$\lambda(T)\partial_x T(\mathbf{x}, t) = -\alpha_h \left(T(\mathbf{x}, t) - T_h^{lo}\right), \qquad x = L_s \tag{3b}$$
$$\lambda(T)\partial_y T(\mathbf{x}, t) = \alpha_{ig} \left(T(\mathbf{x}, t) - T_{ig}(x)\right), \qquad y = 0 \tag{3c}$$
$$\lambda(T)\partial_y T(\mathbf{x}, t) = -\alpha_{ig} \left(T(\mathbf{x}, t) - T_{ig}(x)\right), \qquad y = W_s \tag{3d}$$

with the convective heat transfer coefficients α_h and α_{ig} in W/(m^2 K). In (3), $T_h^\diamondsuit$ in K, $\diamondsuit \in \{up, lo\}$ describe the temperature of the upper and lower specimen holder and $T_{ig}(x)$ (K) is the quasi-stationary temperature profile of the inert gas along the specimen length. The consistent initial condition is defined as $T(\mathbf{x}, 0) = T_0(\mathbf{x})$ for $\mathbf{x} \in \mathrm{cl}(\Omega)$.

The radiative heat flux $\dot{q}_r(\mathbf{x}, T, \mathbf{u}, \eta)$ is calculated using the net radiation method (Siegel and Howell, 2002). For this calculation, the domain Ω is spatially discretized into $N_s = N_x N_y$ equal rectangular elements which are used for the computation of an exchange factor matrix $\mathbf{F}^s(\eta)$. In addition to direct view paths, the matrix $\mathbf{F}^s(\eta)$ captures specular and diffuse reflections depending on the actual position of the specimen with respect to the IR-lamps and the enclosing furnace walls. For fast evaluation, $\mathbf{F}^s(\eta_n)$ is computed and stored for $N_\eta + 1$ fixed positions $\eta_n = -\bar{\eta} + (n-1)\mathrm{d}\eta$ with $d\eta = 2\bar{\eta}/N_\eta$ and $n = 1, \dots, N_\eta + 1$ in advance by means of the hemicube method (Cohen and Greenberg, 1985) using the FE software Ansys. When evaluating the model, $\mathbf{F}^s(\eta)$ is then obtained from the predetermined values by linear interpolation.

A bijective mapping $(i, j) \mapsto k := i + N_x(j-1)$, $\mathbf{x}_k = (x_i, y_j)$ for $i = 1, \dots, N_x$ and $j = 1, \dots, N_y$ allows to assemble the temperature vector $\mathbf{T}(t) = [T(\mathbf{x}_k, t)]_{k=1,\dots,N_s}$. Consequently, the heat flux vectors follow as $\dot{\mathbf{q}}_r(\mathbf{T}, \mathbf{u}, \eta) = [\dot{q}_r(\mathbf{x}_k, T, \mathbf{u}, \eta)]_{k=1,\dots,N_s}$, $\dot{\mathbf{q}}_c(\mathbf{T}) = [\dot{q}_c(\mathbf{x}_k, T)]_{k=1,\dots,N_s}$, and $\dot{\mathbf{q}}_h(\mathbf{T}) = [\dot{q}_h(\mathbf{x}_k, T)]_{k=1,\dots,N_s}$. The radiative net heat flux is thus computed according to, (see (Jadachowski et al., 2017b) for more details),

$$\dot{\mathbf{q}}_r(\mathbf{T}, \mathbf{u}, \eta) = \mathbf{P}_1(\eta) \begin{bmatrix}\mathbf{T}^4 \\ \mathbf{T}_w^4\end{bmatrix} + \mathbf{P}_2(\eta) \begin{bmatrix}\mathbf{u}_h \\ \mathbf{u}_v\end{bmatrix}, \tag{4}$$

where the matrices $\mathbf{P}_1(\eta) = \mathbf{P}_{11}(\eta) - \mathbf{P}_{12}(\eta)\mathbf{P}_{32}^{-1}(\eta)\mathbf{P}_{31}(\eta)$ and $\mathbf{P}_2(\eta) = \mathbf{P}_{12}(\eta)\mathbf{P}_{32}^{-1}(\eta)$ are defined by

$$\begin{bmatrix}\mathbf{P}_{11}(\eta) & \mathbf{P}_{12}(\eta) \\ \mathbf{P}_{21}(\eta) & \mathbf{P}_{22}(\eta) \\ \mathbf{P}_{31}(\eta) & \mathbf{P}_{32}(\eta)\end{bmatrix} = \begin{matrix}\mathrm{diag}\{\boldsymbol{\varepsilon}\}(\mathbf{I} - \mathbf{F}^s(\eta)\mathrm{diag}\{\boldsymbol{\rho}^d\})^{-1} \\ \times(\mathbf{I} - \mathbf{F}^s(\eta) + \mathbf{F}^s(\eta)\mathrm{diag}\{\boldsymbol{\rho}^s\})\sigma.\end{matrix} \tag{5}$$

The submatrices $\mathbf{P}_{ij}(\eta)$, $i = 1, 2, 3$, $j = 1, 2$ capture the radiative interaction in the furnace chamber depending on the specimen position $\eta(t)$. In (4), $\mathbf{T}_w$ contains the surface temperatures of N_w sections of the enclosing furnace walls, which are assumed to be known. The emissivities are assembled in the vector $\boldsymbol{\varepsilon}$; $\boldsymbol{\rho}^d$ and $\boldsymbol{\rho}^s$ describe the diffuse and specular parts of the reflectivity with $\boldsymbol{\varepsilon} + \boldsymbol{\rho}^d + \boldsymbol{\rho}^s = \mathbf{1}$ (Modest, 2003); σ is the Stefan-Boltzmann constant.

The other two heat fluxes $\dot{\mathbf{q}}_c(\mathbf{T})$ and $\dot{\mathbf{q}}_h(\mathbf{T})$ are directly given by Newton's law of cooling

$$\begin{aligned}\dot{\mathbf{q}}_c(\mathbf{T}) &= \alpha_{ig}\left(\mathbf{I}_c\mathbf{T}(t) - \mathbf{T}_{ig}\right) \\ \dot{\mathbf{q}}_h(\mathbf{T}) &= \alpha_h\left(\mathbf{I}_h\mathbf{T}(t) - \mathbf{T}_h\right).\end{aligned} \tag{6}$$

Here, diagonal matrices $\mathbf{I}_c$ and $\mathbf{I}_h$, where the latter has selected diagonal entries being 0, arise from the effective contact regions between the specimen and the holder flanges. The vector $\mathbf{T}_{ig}$ follows from the calculation of the quasi-stationary mean temperature of the inert gas along the coordinate x. The temperatures of the upper and lower specimen holders are assembled in $\mathbf{T}_h$.

For evaluation of the model, finite differences are used with $N_s = 442$ states. Hence, this model is referred to as full-state FD model and is mainly used for simulation purposes.

2.2. Reduced-order FE-model of an oscillating specimen

In view of the relatively high order $N_s = 442$, the FD model is computationally too expensive to serve for controller and observer design. In this paper, a FE approximation with a coarser discretization in space and non-uniform element sizes is used to obtain a lower-order model. Rötzer et al. (2017) compared three approaches for a finite-dimensional approximation of (1)–(3) in terms of model order and accuracy. An overview of model reduction methods is given, e.g., in (Antoulas, 2005).

Following Jadachowski et al. (2017a), 2D hat functions $\boldsymbol{\varphi}(\mathbf{x}) = [\varphi_k(\mathbf{x})]_{k=1,\dots,\tilde{N}_s}$, $\tilde{N}_s \ll N_s$, with a non-uniform support are used to approximate the solution of (1)–(3) by

$$T(\mathbf{x}, t) = \boldsymbol{\theta}^{\mathrm{T}}(t)\boldsymbol{\varphi}(\mathbf{x}), \quad \boldsymbol{\theta}(t) = [\theta_k(t)]_{k=1,\dots,\tilde{N}_s}, \tag{7}$$

where $\theta_k(t)$ is the temperature at the grid point k. The substitution of (7) and (3) into the weighted residual weak form (cf. Reddy and Gartling, 2010)

$$\begin{aligned}0 = \int_\Omega \Big(&\rho c_p(T)\partial_t T(\mathbf{x}, t)\varphi_k(\mathbf{x}) + \lambda(T)\nabla T(\mathbf{x}, t)\nabla\varphi_k(\mathbf{x}) \\ &- \dot{q}(\mathbf{x}, T, \mathbf{u}, \eta)\varphi_k(\mathbf{x})\Big)\mathrm{d}\Omega + \oint_\Gamma \varphi_k(\mathbf{x})\lambda(T)\nabla T(\mathbf{x}, t)\mathbf{n}\mathrm{d}s\end{aligned} \tag{8}$$

Post-print version of the article: L. Jadachowski, A. Steinboeck, and A. Kugi, "State estimation and advanced control of the 2D temperature field in an experimental oscillating annealing device", *Control Engineering Practice*, vol. 78, pp. 116–128, 2018, ISSN: 0967-0661. DOI: 10.1016/j.conengprac.2018.06.011

with $\mathrm{d}\Omega = \mathrm{d}x\mathrm{d}y$, the unit normal vector $\mathbf{n}$ on Γ, and the arc length $\mathrm{d}s$ along Γ yields the FE model in the form

$$\rho\mathbf{M}\dot{\boldsymbol{\theta}}(t) = \mathbf{K}\boldsymbol{\theta}(t) + \boldsymbol{\chi}(\boldsymbol{\theta}, \mathbf{u}, \eta) + \boldsymbol{\gamma}(\boldsymbol{\theta}), \quad \boldsymbol{\theta}(0) = \boldsymbol{\theta}_0. \tag{9}$$

$\mathbf{M}$ and $\mathbf{K}$ denote the heat capacity matrix and the conductivity matrix, respectively. The vector $\boldsymbol{\gamma}(\boldsymbol{\theta})$ follows from the boundary conditions (3). For anisotropic specimen materials, $\mathbf{M}$ and $\mathbf{K}$ may depend on the temperature $\boldsymbol{\theta}$ and on the spatial coordinates $\mathbf{x}$. However, they are assumed constant for the observer and controller design in the remainder of this paper.

The components of the heat flux vector $\boldsymbol{\chi}(\boldsymbol{\theta}, \mathbf{u}, \eta) = [\chi_k(\boldsymbol{\theta}, \mathbf{u}, \eta)]_{k=1,\dots,\tilde{N}_s}$ from (9) are defined in the form

$$\chi_k(\boldsymbol{\theta}, \mathbf{u}, \eta) = \int_\Omega \dot{\tilde{q}}(\mathbf{x}, \mathbf{M}_\theta\boldsymbol{\theta}, \mathbf{u}, \eta)\varphi_k(\mathbf{x})\mathrm{d}\Omega. \tag{10}$$

In (10), $\dot{\tilde{q}}(\mathbf{x}, \mathbf{T}, \mathbf{u}, \eta)$ denotes a piecewise constant spatial approximation of (2), i.e.,

$$\dot{\tilde{q}}(\mathbf{x}, \mathbf{T}, \mathbf{u}, \eta) = -\frac{1}{B_s}\boldsymbol{H}^{\mathrm{T}}(\mathbf{x})\left(\dot{\mathbf{q}}_r(\mathbf{T}, \mathbf{u}, \eta) + \dot{\mathbf{q}}_c(\mathbf{T}) + \dot{\mathbf{q}}_h(\mathbf{T})\right)$$

with a vector $\boldsymbol{H}(\mathbf{x}) = [H_k(\mathbf{x})]_{k=1,\dots,N_s}$. By means of the bijective mapping from Section 2.1, $H_k(\mathbf{x}) = 1$ if $(i-1)L_s/N_x < x \leq iL_s/N_x \wedge (j-1)W_s/N_y < y \leq jW_s/N_y$, and $H_k(\mathbf{x}) = 0$ else, $i = 1, \dots, N_x$ and $j = 1, \dots, N_y$. To compute $\mathbf{T}(t)$, (7) is evaluated at the grid point $\mathbf{x}_k$, which yields the expression $\mathbf{T}(t) = \mathbf{M}_\theta\boldsymbol{\theta}(t)$ with the mapping matrix $\mathbf{M}_\theta = \left[\boldsymbol{\varphi}^{\mathrm{T}}(\mathbf{x}_k)\right]_{k=1,\dots,N_s} \in \mathbb{R}^{N_s \times \tilde{N}_s}$ as used in (10).

2.3. Time averaging

In this section, model averaging (Khalil, 2002) is used to obtain a real-time executable model that can serve as a basis for observer and controller design. The time averaging method is applied to make (9) independent of $\eta(t)$. That is, the oscillatory specimen motion is taken into account in an averaged manner. Time averaging is also considered by Jadachowski et al. (2018) for the determination of an optimal feedforward control.

Let Π be the period of the periodic specimen oscillations, i.e., $\eta(t) = \eta(t - \Pi)$. In a first step, it is assumed that $\tau \gg \Pi$, where τ is the minimal time constant of the linearization of (9). Because of this assumption and because of the small amplitude $\bar{\eta}$, it is postulated that the effect of the periodic specimen motion $\eta(t)$ on the temporal evolution of the mean specimen temperature is only weak. However, the periodic motion does have an influence on the spatial distribution of the specimen temperature.

Based on the former analysis about the effect and the time scale of $\eta(t)$, a time-average model

$$\begin{aligned}\dot{\boldsymbol{\theta}}_{\mathrm{av}}(t) &= \mathbf{f}(\boldsymbol{\theta}_{\mathrm{av}}, \mathbf{u}) \\ &= (\rho\mathbf{M})^{-1}\left(\mathbf{K}\boldsymbol{\theta}_{\mathrm{av}}(t) + \boldsymbol{\chi}_{\mathrm{av}}(\boldsymbol{\theta}_{\mathrm{av}}, \mathbf{u}) + \boldsymbol{\gamma}(\boldsymbol{\theta}_{\mathrm{av}})\right)\end{aligned} \tag{11a}$$

with

$$\boldsymbol{\chi}_{\mathrm{av}}(\boldsymbol{\theta}_{\mathrm{av}}, \mathbf{u}) = \frac{1}{\Pi}\int_t^{t+\Pi} \boldsymbol{\chi}(\boldsymbol{\theta}_{\mathrm{av}}, \mathbf{u}, \eta(t))\mathrm{d}t \tag{11b}$$

and the initial condition $\boldsymbol{\theta}_{\mathrm{av}}(0) = \boldsymbol{\theta}(0)$ approximates the time-varying model (9). With (11), a time-invariant reduced-order FE model of the temperature field in the oscillating specimen is available. A discrete-time formulation of this model will serve as a basis for the estimation of 2D temperature profiles in Section 3.

Remark 1. Formally, a crucial problem in model averaging is to analyze and prove the approximation order of (11) compared to (9). In (Khalil, 2002), this is typically addressed by a state transformation $\boldsymbol{\theta}(t) = \boldsymbol{\theta}_{\mathrm{av}}(t) + \boldsymbol{\zeta}(t, \boldsymbol{\theta}_{\mathrm{av}})$ with a Π-periodic function $\boldsymbol{\zeta}(t, \boldsymbol{\theta}) = \int_0^t [\boldsymbol{\chi}(\boldsymbol{\theta}, \mathbf{u}, \eta(s)) - \boldsymbol{\chi}_{\mathrm{av}}(\boldsymbol{\theta}, \mathbf{u})]\,\mathrm{d}s$ to express (9) as a perturbation of the average model (11). In case of the nonlinear model (11) with numerically determined values $\mathbf{M}$, $\mathbf{K}$, and $\boldsymbol{\chi}(\boldsymbol{\theta}, \mathbf{u}, \eta)$, this proof is highly non-trivial and thus not considered in this paper.

Remark 2. Instead of averaging the ODE (9), one may consider time averaging of the PDE (1) as shown by Matthies (2001). In (Matthies, 2001), parabolic PDEs with time-periodic perturbations are approximated up to exponentially small errors. In particular, the originally non-autonomous PDE is transformed such that the non-autonomous terms are exponentially small in the period of the acting input. Besides the fact that (1) constitutes a non-linear partial integro-differential equation, which induces additional challenges, note that due to the complex furnace geometry and multiple reflections occurring on specular surfaces, $\dot{q}(\mathbf{x}, T, \mathbf{u}, \eta)$ in (1) cannot be analytically expressed, not even for $\eta(t) \equiv 0$. Hence, (1) has to be discretized and approximated by the ODE (9) and consequently the averaging methods for ODEs are employed in this work.

2.4. Model validation

Model parameters were identified by Jadachowski et al. (2017b) on the basis of the full-order FD model with the fixed specimen position $\eta(t) \equiv 0$. In (Jadachowski et al., 2017b), the emissivities of the specimen and the enclosure walls as well as the convective heat transfer coefficients α_h and α_{ig} were identified based on step responses of two horizontal IR-lamps. Local temperature measurements of three thermocouples were recorded during the heating period of 400 s. Additionally, 2D images of the surface temperature of the specimen were taken at discrete times using a temporarily installed CCD thermocamera. For these snapshots, the vertical reflector and lamps were temporarily folded to the side, i.e., the images were captured through the quartz glass window, see Fig. 1.

For parameter estimation, a minimization problem was solved that takes into account both the time evolutions of local thermocouple measurements and the 2D images of spatial temperature fields. The result of this minimization problem was $\varepsilon_s = 0.90$ for the specimen emissivity, $\varepsilon_w = 0.32$ for emissivities of furnace walls, and $\alpha_h = 142.6\,\mathrm{W/(m^2\,K)}$ and $\alpha_{ig} = 13.3\,\mathrm{W/(m^2\,K)}$ for the heat

Post-print version of the article: L. Jadachowski, A. Steinboeck, and A. Kugi, "State estimation and advanced control of the 2D temperature field in an experimental oscillating annealing device", *Control Engineering Practice*, vol. 78, pp. 116–128, 2018, ISSN: 0967-0661. DOI: 10.1016/j.conengprac.2018.06.011

transfer coefficients. It was found that the relative accuracy of the model with the identified parameters is better than 4.4 % of the maximum measured temperature.

The identified parameters are also used in this paper. Material parameters and the remaining radiative parameters are taken from (Incropera et al., 2007), see, (Jadachowski et al., 2017b).

3. Observer design

In this section, the estimation of the spatial temperature evolution by an EKF is considered. The EKF uses measurements of the local surface temperatures of the specimen that are recorded by thermocouples (TCs). The placement of these thermocouples with the coordinates $\boldsymbol{\xi} = (x, y)$ is discussed in the next subsection.

3.1. Temperature measurements

Four TCs are used to measure the surface temperature of the specimen. The TCs are mounted at four distinct points on the specimen surface shown in Fig. 2. The thermocouples TC1, TC2, and TC3 are located

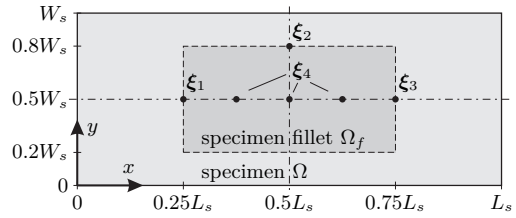

Figure 2: Four thermocouples mounted on the specimen surface.

at the fixed positions $\boldsymbol{\xi}_1 = (0.25L_s, 0.5W_s)$, $\boldsymbol{\xi}_2 = (0.5L_s, 0.8W_s)$, and $\boldsymbol{\xi}_3 = (0.75L_s, 0.5W_s)$, respectively. The measurements of these TCs are used by the EKF. The position $\boldsymbol{\xi}_4$ of the thermocouple TC4 varies between the experiments and is taken from the set $\boldsymbol{\xi}_4 \in \{(0.375L_s, 0.5W_s), (0.5L_s, 0.5W_s), (0.625L_s, 0.5W_s)\}$.

Since the temperature field in the area of the specimen fillet is of particular importance, only TC positions in Ω_f are considered. Temperature measurements $\Theta_i(t)$, $i = 1, \ldots, 4$ obtained from the four TCs are recorded with the sampling time t_s and assembled in $\mathbf{y}_j = [\Theta_i(jt_s)]_{i=1,\ldots,3}$ and $y_{r,j} = \Theta_4(jt_s)$. Apart from these measurements, no other sensor signals are used for the estimation of the temperature evolution of the specimen during furnace operation.

Remark 3. The selection of the TC positions with $\boldsymbol{\xi}_4 = (0.5L_s, 0.5W_s)$ resembles results of an optimization-based algorithm for sensor placement as reported by Rötzer et al. (2017). Therein, the problem of optimal sensor placement was solved by maximizing the Gramian determinant (cf. Vande Wouwer et al., 2000), which was calculated on the basis of a model discretized with global trial functions. Similar results are expected when using the local trial functions $\boldsymbol{\varphi}(\mathbf{x})$.

3.2. EKF design

Prior to the EKF design, the forward Euler method is applied to (11) to obtain the discrete-time dynamics

$$\boldsymbol{\theta}_{\mathrm{av},j+1} = \mathbf{F}(\boldsymbol{\theta}_{\mathrm{av},j}, \mathbf{u}_j) + \mathbf{w}_j, \quad \boldsymbol{\theta}_{\mathrm{av},0} = \boldsymbol{\theta}_{\mathrm{av}}(0), \tag{12a}$$

with $\boldsymbol{\theta}_{\mathrm{av},j} = \boldsymbol{\theta}_{\mathrm{av}}(jt_s)$, $\mathbf{u}_j = \mathbf{u}(jt_s)$, and $\mathbf{F}(\boldsymbol{\theta}_{\mathrm{av},j}, \mathbf{u}_j) = \boldsymbol{\theta}_{\mathrm{av},j} + t_s\mathbf{f}(\boldsymbol{\theta}_{\mathrm{av},j}, \mathbf{u}_j)$, $j \in \mathbb{N}_0$. The state equation is augmented with the process noise $\mathbf{w}_j \in \mathbb{R}^{\tilde{N}_s}$. The temperature evaluations at the TC positions read as

$$\mathbf{y}_j = \mathbf{C}\boldsymbol{\theta}_{\mathrm{av},j} + \mathbf{v}_j, \tag{12b}$$

with $\mathbf{C} = [\boldsymbol{\varphi}(\boldsymbol{\xi}_1)\ \boldsymbol{\varphi}(\boldsymbol{\xi}_2)\ \boldsymbol{\varphi}(\boldsymbol{\xi}_3)]^{\mathrm{T}}$ and the measurement noise $\mathbf{v}_j \in \mathbb{R}^3$. With (12b), only the three TC measurements at the positions $\boldsymbol{\xi}_i$, $i = 1, 2, 3$ are available to the EKF. The remaining measured value $y_{r,j}$ at $\boldsymbol{\xi}_4$ is used for validation of the observer.

It is assumed that $\mathbf{w}_j$ and $\mathbf{v}_j$ are normally distributed white noise sequences with zero mean and positive definite covariance matrices $\hat{\mathbf{Q}}$ and $\hat{\mathbf{R}}$, respectively. The weighting matrices $\hat{\mathbf{Q}}$ and $\hat{\mathbf{R}}$ are empirically determined in the form $\hat{\mathbf{Q}} = \hat{q}_0\big(\hat{q}_1 \mathrm{sign}(\mathbf{M}) + \mathbf{1}_{\tilde{N}_s}\mathbf{1}_{\tilde{N}_s}^{\mathrm{T}}\big)^2$ and $\hat{\mathbf{R}} = \hat{r}_0\mathbf{I}$ with the design parameters $\hat{q}_0$, $\hat{q}_1$, $\hat{r}_0 > 0$. For the EKF design, the discrete-time input sequence $\mathbf{u}_j = \mathbf{u}(jt_s)$ is assumed to be known, e.g., from the controller presented in Section 4.

According to the EKF design, see, e.g., (Simon, 2006), the estimate $\hat{\boldsymbol{\theta}}_j$ of the specimen temperature is given by

$$\hat{\boldsymbol{\theta}}_j = \hat{\boldsymbol{\theta}}_j^- + \hat{\mathbf{L}}_j\left(\mathbf{y}_j - \mathbf{C}\hat{\boldsymbol{\theta}}_j^-\right) \tag{13}$$

with the Kalman gain $\hat{\mathbf{L}}_j = \hat{\mathbf{P}}_j\mathbf{C}^{\mathrm{T}}\left(\mathbf{C}\hat{\mathbf{P}}_j\mathbf{C}^{\mathrm{T}} + \hat{r}_0\mathbf{I}\right)^{-1}$. After each measurement, the so-called a priori estimate $\hat{\boldsymbol{\theta}}_j^-$ is propagated using the system dynamics (12a), i.e.,

$$\hat{\boldsymbol{\theta}}_{j+1}^- = \mathbf{F}(\hat{\boldsymbol{\theta}}_j, \mathbf{u}_j). \tag{14}$$

The observer error covariance matrix $\hat{\mathbf{P}}_j$ is updated by the solution of the discrete-time Riccati equation

$$\hat{\mathbf{P}}_{j+1} = \hat{\boldsymbol{\Phi}}_j\left(\mathbf{I} - \hat{\mathbf{L}}_j\mathbf{C}\right)\hat{\mathbf{P}}_j\hat{\boldsymbol{\Phi}}_j^{\mathrm{T}} + \hat{\mathbf{Q}}. \tag{15}$$

The determination of $\hat{\mathbf{P}}_j$ is based on a linearization of (12a) at the current state estimate $\hat{\boldsymbol{\theta}}_j$

$$\hat{\boldsymbol{\Phi}}_j = \left.\frac{\partial\mathbf{F}(\boldsymbol{\theta}_{\mathrm{av},j}, \mathbf{u}_j)}{\partial\boldsymbol{\theta}_{\mathrm{av},j}}\right|_{\boldsymbol{\theta}_{\mathrm{av},j}=\hat{\boldsymbol{\theta}}_j}. \tag{16}$$

The definition of suitable conditions for the initial temperature estimate $\hat{\boldsymbol{\theta}}_0$ and the initial covariance matrix $\hat{\mathbf{P}}_0$ completes the design of the EKF.

4. Temperature tracking control

In this section, a control strategy is proposed to realize a transition of the mean fillet temperature along the desired

Post-print version of the article: L. Jadachowski, A. Steinboeck, and A. Kugi, "State estimation and advanced control of the 2D temperature field in an experimental oscillating annealing device", *Control Engineering Practice*, vol. 78, pp. 116–128, 2018, ISSN: 0967-0661. DOI: 10.1016/j.conengprac.2018.06.011

trajectory $T_{\mathrm{ref}}(t)$ with minimal temperature inhomogeneity. A promising and well-known approach for tracking control is a two-degree-of-freedom control concept, i.e.,

$$\mathbf{u}_j = \mathbf{u}_j^{\mathrm{ff}} + \Delta\mathbf{u}_j, \quad j \geq 0 \tag{17}$$

comprising a feedforward part $\mathbf{u}_j^{\mathrm{ff}}$ and a feedback part $\Delta\mathbf{u}_j$. For the considered furnace, three feedforward control strategies using dynamic optimization were developed and compared by Jadachowski et al. (2018). By assuming nominal furnace conditions, one of these controllers is employed here to obtain the reference signals $\mathbf{u}_j^{\mathrm{ff}}$ of the system input that ensure the desired transition of the mean temperature. Reference signals $\boldsymbol{\theta}_{\mathrm{ref},j}$ of the corresponding spatial temperature profiles follow from an evaluation of (12) with $\mathbf{u}_j = \mathbf{u}_j^{\mathrm{ff}}$, $\mathbf{w}_j = \mathbf{0}$, and $\mathbf{v}_j = \mathbf{0}$. The feedback term $\Delta\mathbf{u}_j$ is introduced to compensate for model mismatches and parameter uncertainties. It is based on an LQG control concept presented in Section 4.2 and uses the previously calculated temperature estimates $\hat{\boldsymbol{\theta}}_j$.

4.1. Optimal feedforward control

In this section, the feedforward control input $\mathbf{u}_j^{\mathrm{ff}} = [u_{i,j}^{\mathrm{ff}}]_{i=1,\dots,N_v+N_h}$ is calculated by dynamic optimization on the basis of the discrete-time dynamics (12) of the time-averaged FE model (11). The feedforward control input is chosen as

$$\mathbf{u}_j^{\mathrm{ff}} = \mathrm{sat}(v_j \mathbf{u}_c), \tag{18}$$

with $\mathbf{u}_c = [u_{c,i}]_{i=1,\dots,N_v+N_h}$, where the evaluation of the saturation function $\mathrm{sat}(v_j u_{c,i}) = 0$ for $v_j u_{c,i} < 0$, $\mathrm{sat}(v_j u_{c,i}) = \bar{u}$ if $v_j u_{c,i} \geq \bar{u}$, and $\mathrm{sat}(v_j u_{c,i}) = v_j u_{c,i}$ else, is applied componentwise. The feedforward controller (18) amplifies the constant power distribution $\mathbf{u}_c \in \mathbb{R}^{N_h+N_v}$ by a time-dependent scalar value $v_j = v(jt_s)$. The control variables are both v_j and $\mathbf{u}_c$.

By introducing the mean temperature of the specimen fillet $\tilde{T}(\boldsymbol{\theta}_{\mathrm{av},j}) = \mathbf{c}_m^{\mathrm{T}} \boldsymbol{\theta}_{\mathrm{av},j}$ with $\mathbf{c}_m = \int_{\Omega_f} \boldsymbol{\varphi}(\mathbf{x}) \mathrm{d}\Omega / A_f$ and its deviation

$$e_j(\boldsymbol{\theta}_{\mathrm{av},j}) = \tilde{T}(\boldsymbol{\theta}_{\mathrm{av},j}) - T_{\mathrm{ref},j} \tag{19}$$

from the reference trajectory $T_{\mathrm{ref},j} = T_{\mathrm{ref}}(jt_s)$, (18) is calculated from the solution of the constrained discrete-time optimal control problem (OCP)

$$\begin{aligned}
\underset{\substack{\mathbf{v}_j \in \\ \mathbb{R}^{N_h+N_v+1}}}{\text{minimize}} \quad & \sum_{j=0}^{N-1} \left(g_0 e_j^2(\boldsymbol{\theta}_{\mathrm{av},j}) + g_1 \kappa_j(\boldsymbol{\theta}_{\mathrm{av},j}) \right) && \text{(20a)} \\
\text{s. t.} \quad & \boldsymbol{\theta}_{\mathrm{av},j+1} = \mathbf{F}(\boldsymbol{\theta}_{\mathrm{av},j}, \mathrm{sat}(v_j \mathbf{u}_c)) && \text{(20b)} \\
& \boldsymbol{\theta}_{\mathrm{av},0} = \boldsymbol{\theta}_0 && \text{(20c)} \\
& \max(\mathbf{u}_c) = \bar{u} && \text{(20d)} \\
& \mathbf{0} \leq \mathbf{u}_c \leq \bar{u} \mathbf{1}_{N_v+N_h}. && \text{(20e)}
\end{aligned}$$

Here, $g_0,\ g_1 > 0$ denote weighting parameters and $\mathbf{v}_j^{\mathrm{T}} = \begin{bmatrix} v_j & \mathbf{u}_c^{\mathrm{T}} \end{bmatrix}$ are optimization variables. While the first term in (20a) aims at a desired tracking performance, the second term with

$$\begin{aligned}
\kappa_j(\boldsymbol{\theta}_{\mathrm{av},j}) &= \frac{1}{A_f} \int_{\Omega_f} \left(\boldsymbol{\theta}_{\mathrm{av},j}^{\mathrm{T}} \boldsymbol{\varphi}(\mathbf{x}) - \tilde{T}(\boldsymbol{\theta}_{\mathrm{av},j}) \right)^2 \mathrm{d}\Omega \\
&= \boldsymbol{\theta}_{\mathrm{av},j}^{\mathrm{T}} \mathbf{W} \boldsymbol{\theta}_{\mathrm{av},j}
\end{aligned} \tag{21}$$

and $\mathbf{W} = \int_{\Omega_f} \boldsymbol{\varphi}(\mathbf{x}) \boldsymbol{\varphi}^{\mathrm{T}}(\mathbf{x}) \mathrm{d}\Omega / A_f - \mathbf{c}_m \mathbf{c}_m^{\mathrm{T}}$ corresponds to the control objective of a uniform specimen temperature.

The OCP (20) uses the horizon length βt_E with a design parameter $\beta > 1$. The variable t_E denotes the transition time between two steady-state values of $T_{\mathrm{ref}}(t)$. Hence, $N = \lceil \beta t_E / t_s \rceil \in \mathbb{N}_+$ is chosen in (20a). The condition $\beta > 1$ is justified by the still evolving value of $\kappa_j(\boldsymbol{\theta}_{\mathrm{av},j})$ for $t \geq t_E$ and helps to reduce the temperature inhomogeneity for $t > t_E$.

Remark 4. The parametrization (18) represents a restriction for the parametric optimization problem (20). Hence, the solution of (20) may be sub-optimal compared to the solution of an OCP that directly optimizes the input sequence $\mathbf{u}_j^{\mathrm{ff}}$. However, the sacrificed control performance is rewarded by lower computational costs as shown by Jadachowski et al. (2017a) for the furnace model (9) with the fixed specimen position $\eta(t) \equiv 0$. In case of the oscillating specimen, an OCP based on the time-varying model would require a much finer time discretization. Then, the expected reduction of the computational effort associated with the input parametrization (18) is even more significant.

The OCP (20) is solved by means of the open source software IPOPT (Wächter and Biegler, 2006). It uses an interior-point line-search algorithm to compute solutions of large-scale nonlinear programming problems. The solution of (20) is followed by the determination of the feedback signal $\Delta\mathbf{u}_j$ in the next subsection.

4.2. LQG feedback control

Because of possible unmodeled furnace disturbances, parameter uncertainties, or model-plant mismatches, the specimen temperature may deviate from the reference evolution. In terms of the time-average reduced-order system state, this means that $\boldsymbol{\theta}_{\mathrm{av},j}$ can deviate from $\boldsymbol{\theta}_{\mathrm{ref},j}$. Because $\boldsymbol{\theta}_{\mathrm{av},j}$ cannot be directly measured, its estimated counterpart $\hat{\boldsymbol{\theta}}_j$ is used for control. The same applies to the mean temperature $\tilde{T}(\boldsymbol{\theta}_{\mathrm{av},j})$ of the specimen fillet, which is thus replaced in the controller by $\tilde{T}(\hat{\boldsymbol{\theta}}_j) = \mathbf{c}_m^{\mathrm{T}} \hat{\boldsymbol{\theta}}_j$. In this paper, an LQG controller is employed for feedback tracking control. Its task is to minimize the estimated control error $\hat{\boldsymbol{\theta}}_j - \boldsymbol{\theta}_{\mathrm{ref},j}$.

To ensure that the estimated mean steady-state temperature error $e_j(\hat{\boldsymbol{\theta}}_j)$ vanishes, the LQG control concept is augmented by an integral control action. In a discrete-time formulation, the integrated mean temperature error $e_{I,j}$ follows the dynamics

$$e_{I,j+1} = e_{I,j} + \delta(\mathbf{u}_j) t_s e_j(\hat{\boldsymbol{\theta}}_j), \quad e_{I,0} = 0, \tag{22}$$

Post-print version of the article: L. Jadachowski, A. Steinboeck, and A. Kugi, "State estimation and advanced control of the 2D temperature field in an experimental oscillating annealing device", *Control Engineering Practice*, vol. 78, pp. 116–128, 2018, ISSN: 0967-0661. DOI: 10.1016/j.conengprac.2018.06.011

with $e_j(\hat{\boldsymbol{\theta}}_j)$ from (19). With the augmented error state $\mathbf{e}_j = \left[\hat{\boldsymbol{\theta}}_j^{\mathrm{T}} - \boldsymbol{\theta}_{\mathrm{ref},j}^{\mathrm{T}} \;\; e_{I,j}\right]^{\mathrm{T}}$ and the linearizations

$$\boldsymbol{\Phi}_j = \left.\frac{\partial \mathbf{F}(\boldsymbol{\theta}_{\mathrm{av},j}, \mathbf{u}_j^{\mathrm{ff}})}{\partial \boldsymbol{\theta}_{\mathrm{av},j}}\right|_{\boldsymbol{\theta}_{\mathrm{av},j}=\boldsymbol{\theta}_{\mathrm{ref},j}} \tag{23a}$$

$$\boldsymbol{\Gamma}_j = \left.\frac{\partial \mathbf{F}(\boldsymbol{\theta}_{\mathrm{ref},j}, \mathbf{u}_j)}{\partial \mathbf{u}_j}\right|_{\mathbf{u}_j=\mathbf{u}_j^{\mathrm{ff}}} \tag{23b}$$

along the predetermined reference trajectories $\boldsymbol{\theta}_{\mathrm{ref},j}$ and $\mathbf{u}_j^{\mathrm{ff}}$, satisfying $T_{\mathrm{ref},j} = \mathbf{c}_m^{\mathrm{T}}\boldsymbol{\theta}_{\mathrm{ref},j}$, the linearized error dynamics

$$\mathbf{e}_{j+1} = \underbrace{\begin{bmatrix} \boldsymbol{\Phi}_j & 0 \\ \delta(\mathbf{u}_j) t_s \mathbf{c}_m^{\mathrm{T}} & 1 \end{bmatrix}}_{\tilde{\boldsymbol{\Phi}}_j} \mathbf{e}_j + \underbrace{\begin{bmatrix} \boldsymbol{\Gamma}_j \\ 0 \end{bmatrix}}_{\tilde{\boldsymbol{\Gamma}}_j} \Delta\mathbf{u}_j \tag{24}$$

serves as a basis for the design of the feedback controller. Note that the calculation of $\boldsymbol{\Phi}_j$ in (23a) is based on $\boldsymbol{\theta}_{\mathrm{ref},j}$ and $\mathbf{u}_j^{\mathrm{ff}}$, while $\hat{\boldsymbol{\Phi}}_j$ computed in (16) uses $\hat{\boldsymbol{\theta}}_j$ and $\mathbf{u}_j = \mathbf{u}_j^{\mathrm{ff}} + \Delta\mathbf{u}_j$.

Remark 5. In (22), $\delta(\mathbf{u}_j)$ is used to prevent integrator windup effects in case of input saturations. It is chosen in the form $\delta(\mathbf{u}_j) = 0$ if $\mathbf{1}_{N_v+N_h}^{\mathrm{T}}\mathbf{u}_j > \delta_0$, and $\delta(\mathbf{u}_j) = 1$ else, with a design parameter $\delta_0 > 0$. Other anti-windup strategies can be found, e.g., in (Hippe, 2006).

Following Franklin et al. (1997), the feedback control law

$$\Delta\mathbf{u}_j = \mathbf{K}_j\mathbf{e}_j, \quad \forall j = 0, \ldots, N-1, \tag{25}$$

with the time-varying control gain matrix

$$\mathbf{K}_j = -\left(r_0\mathbf{I} + \tilde{\boldsymbol{\Gamma}}_j^{\mathrm{T}}\mathbf{P}_{j+1}\tilde{\boldsymbol{\Gamma}}_j\right)^{-1}\left(\tilde{\boldsymbol{\Gamma}}_j^{\mathrm{T}}\mathbf{P}_{j+1}\tilde{\boldsymbol{\Phi}}_j\right) \tag{26}$$

minimizes the cost function

$$J = \frac{1}{2}\sum_{j=0}^{N-1}\left(\mathbf{e}_j^{\mathrm{T}}\mathbf{Q}\mathbf{e}_j + r_0\Delta\mathbf{u}_j^{\mathrm{T}}\Delta\mathbf{u}_j\right). \tag{27}$$

$\mathbf{Q}$ is a user-defined symmetric positive semidefinite weighting matrix, chosen in the form

$$\mathbf{Q} = \begin{bmatrix} q_0\mathbf{c}_m\mathbf{c}_m^{\mathrm{T}} & \mathbf{0} \\ \mathbf{0}^{\mathrm{T}} & q_1 \end{bmatrix} \tag{28}$$

with the design parameters $q_0, q_1 > 0$. The first term in (27) simplifies to $\frac{1}{2}\sum_{j=0}^{N-1}(q_0 e_j^2(\hat{\boldsymbol{\theta}}_j) + q_1 e_{I,j}^2)$, i.e., it corresponds to the mean temperature error and its integral value. Additionally, the regularization term $r_0\Delta\mathbf{u}_j^{\mathrm{T}}\Delta\mathbf{u}_j$ in (27) with the penalty parameter $r_0 > 0$ prevents large corrections of the heating power. The parameters q_0, q_1, and r_0 are chosen in such a way that the feedback law (25) mainly adheres to the primary control objective, i.e., to track the desired mean reference temperature.

For the determination of $\mathbf{K}_j$, the backwards evolving discrete Riccati equation

$$\mathbf{P}_j = \mathbf{Q} + \tilde{\boldsymbol{\Phi}}_j^{\mathrm{T}}\mathbf{P}_{j+1}\tilde{\boldsymbol{\Phi}}_j + \left(\tilde{\boldsymbol{\Gamma}}_j^{\mathrm{T}}\mathbf{P}_{j+1}\tilde{\boldsymbol{\Phi}}_j\right)^{\mathrm{T}}\mathbf{K}_j \tag{29}$$

has to be recursively solved for $j = N-1, \ldots, 0$. In (29), $\mathbf{P}_N = \mathbf{P}_S$ is calculated from the solution of the algebraic Riccati equation

$$\mathbf{P}_S = \mathbf{Q} + \tilde{\boldsymbol{\Phi}}_N^{\mathrm{T}}\mathbf{P}_S\tilde{\boldsymbol{\Phi}}_N - \boldsymbol{\Psi}^{\mathrm{T}}\left(r_0\mathbf{I} + \tilde{\boldsymbol{\Gamma}}_N^{\mathrm{T}}\mathbf{P}_S\tilde{\boldsymbol{\Gamma}}_N\right)^{-1}\boldsymbol{\Psi}$$

with $\boldsymbol{\Psi} = \tilde{\boldsymbol{\Gamma}}_N^{\mathrm{T}}\mathbf{P}_S\tilde{\boldsymbol{\Phi}}_N$ obtained by substituting (26) into (29) for $j = N$ and $\mathbf{P}_N = \mathbf{P}_{N+1} = \mathbf{P}_S$.

5. Results from the industrial implementation

To validate the developed estimation and control concepts, a measurement campaign consisting of six annealing cycles was carried out in the considered experimental furnace of voestalpine Stahl GmbH. The purpose of this measurement campaign was threefold. At first, it was aimed to validate the estimation performance of the EKF by comparing temperature recordings of the thermocouple TC4 with the corresponding estimated temperature. Secondly, the tracking performance of the proposed control concept was investigated by comparing the mean specimen temperature with its reference signal. The third purpose was to investigate the effect of the oscillating movement of the specimen on the spatial homogeneity of its temperature field.

For the latter purpose, three experiments were carried out with a fixed specimen position and three with an oscillating specimen. For each of the three experiments, the position $\boldsymbol{\xi}_4$ of TC4 was modified and selected from the set $\{(0.375L_s, 0.5W_s), (0.5L_s, 0.5W_s), (0.625L_s, 0.5W_s)\}$. The positions of the other TCs remained unchanged as defined in Fig. 2 in all six experiments. The TC measurements and the system input signals were recorded during the heating period $[0, 2t_E]$.

The reference signal for the mean specimen temperature was chosen as illustrated in Fig. 3 in all experiments. Here,

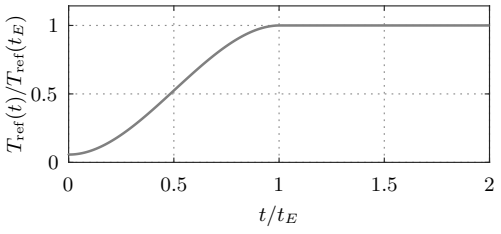

Figure 3: Reference signal for the mean specimen temperature normalized w.r.t. the target temperature at time $t = t_E$.

a piecewise polynomial C^1-function was used for $T_{\mathrm{ref}}(t)$. For $t > t_E$, $T_{\mathrm{ref}}(t)$ was held constant. The reference trajectory realizes a transition starting from the initial mean

Post-print version of the article: L. Jadachowski, A. Steinboeck, and A. Kugi, "State estimation and advanced control of the 2D temperature field in an experimental oscillating annealing device", *Control Engineering Practice*, vol. 78, pp. 116–128, 2018, ISSN: 0967-0661. DOI: 10.1016/j.conengprac.2018.06.011

temperature at $t = 0$ to the desired setpoint temperature for $t \geq t_E$. The considered heating period is twice as long as the transition time t_E. This choice ensures that the experiments also cover the homogenization of the temperature field after the mean temperature has reached its setpoint value $T_{\mathrm{ref}}(t_E)$ at the time t_E.

The measurement campaign was carried out with 8 horizontal IR-lamps h_i, $i \in \{1, \ldots, 4, N_h-3, N_h-2, N_h-1, N_h\}$ and 6 vertical IR-lamps v_i, $i \in \{1, 2, 3, N_v-2, N_v-1, N_v\}$. As investigated by Jadachowski et al. (2017a), the use of additional IR-lamps would not improve the overall control performance. For technical reasons, the IR-lamps are controlled in groups by phase-fired thyristors, i.e., the horizontal IR-lamps by four thyristors $T_1^h = (h_{N_h}, h_{N_h-1})$, $T_2^h = (h_1, h_2)$, $T_3^h = (h_3, h_{N_h-2})$, $T_4^h = (h_4, h_{N_h-3})$, and the vertical IR-lamps by two thyristors $T_1^v = (v_1, v_{N_v})$ and $T_2^v = (v_2, v_3, v_{N_v-2}, v_{N_v-1})$. The remaining lamps were deactivated during the experiments.

5.1. Experiments with a fixed specimen position

Temperature measurements of a representative experiment with a fixed specimen position $\eta(t) \equiv 0$ are presented in Fig. 4. In particular, this figure shows time evolutions of measurements of the experiment with the TC4 located at the position $\boldsymbol{\xi}_4 = (0.5L_s, 0.5W_s)$.

Figure 4(A) shows the estimated relative control error of the mean temperature $e_j(\hat{\boldsymbol{\theta}}_j)/T_{\mathrm{ref}}(t_E)$. The proposed control strategy achieves a high tracking performance in terms of the mean specimen temperature. In the evaluated experiment, the relative mean steady-state control error is below 0.5 %. This good control performance is achieved because of the integral action of the LQG feedback controller and is similar in the remaining two experiments with TC measurements $\Theta_4(t)$ located at $\boldsymbol{\xi}_4 = (0.375L_s, 0.5W_s)$ and at $\boldsymbol{\xi}_4 = (0.625L_s, 0.5W_s)$, respectively. During the transient heating phase, only a minor mean control error below 2 % of the target temperature occurs. This minor error can be attributed to the saturation of the control variables, i.e., more powerful lamps would be necessary to realize the desired temperature transition with even higher accuracy.

The relative local estimation errors $e_{\mathrm{TC}i,j}/T_{\mathrm{ref}}(t_E)$ with $e_{\mathrm{TC}i,j} = \Theta_i(jt_s) - \boldsymbol{\varphi}^{\mathrm{T}}(\boldsymbol{\xi}_i)\hat{\boldsymbol{\theta}}_j$, $i = 1, \ldots, 3$ are shown in Fig. 4(B). The small values of $e_{\mathrm{TC}i,j}$, $i = 1, 2, 3$ arise from the fact that they are used by the EKF for the temperature estimation. For the observer validation, local estimation errors $e_{\mathrm{TC4},j}$ are shown in Fig. 4(C). Here, estimation errors from all three experiments with the changing position $\boldsymbol{\xi}_4$ are compared. During transients, $e_{\mathrm{TC4},j}$ is less than 1.5 % and reduces to 0.5 % of the setpoint value at steady states. This demonstrates a very good estimation performance of the EKF which is essential to achieve the stated control objectives.

To evaluate the temperature homogeneity, a sup-norm

$$T_{\mathrm{sup}}(t) = \max_{(x,y)\in\Omega_f} \left|\hat{T}(x, y, t) - T_{\mathrm{ref}}(t)\right|$$

with $\hat{T}(x, y, t) = \boldsymbol{\varphi}^{\mathrm{T}}(\mathbf{x})\hat{\boldsymbol{\theta}}_j$ is computed. It describes the maximum local deviation between the estimated 2D temperature field $\hat{T}(x, y, t)$ and the reference trajectory $T_{\mathrm{ref}}(t)$ in the specimen fillet. The normalized sup-norm $T_{\mathrm{sup}}(t)/T_{\mathrm{ref}}(t_E)$ w.r.t. the setpoint value is given in Fig. 4(D). The increase of the temperature inhomogeneity for $t < t_E$ is attributed to the saturation of the control inputs in the transient heating phase. For $t > t_E$, when the mean temperature is already nearly constant (cf. Fig. 4(A)), the spatial temperature inhomogeneity continuously decreases and arrives at 4 % of $T_{\mathrm{ref}}(t_E)$.

The time evolutions of the normalized IR-lamp powers $\mathbf{u}_h(t)$ and $\mathbf{u}_v(t)$ are shown in Figs. 4(E) and 4(F), respectively. In particular, Fig. 4(E) presents normalized powers of the horizontal IR-lamps controlled by the four thyristors T_i^h, $i = 1, \ldots, 4$. The highest heating power is emitted by the IR-lamps controlled by the thyristor T_4^h, followed by T_2^h and T_1^h. For the selected reference trajectory and the non-oscillating specimen, T_3^h supplies the lowest power. The thyristors T_4^h and T_2^h saturate during the transient heating phase. This is the main reason for the control error shown in Fig. 4(A) for $t \in (0.5t_E, t_E)$. For $t > t_E$, T_1^h and T_2^h converge to the same steady-state values. This results in a symmetric power distribution w.r.t the plane $x = 0.5L_s$ and, hence, symmetric temperature profiles are expected. The normalized powers of the vertical IR-lamps controlled by the two thyristors T_1^v and T_2^v are shown in Fig. 4(F). Again, the highest heating power is emitted by the outermost IR-lamps controlled by the thyristor T_1^v. This thyristor saturates in the transient heating phase $t < t_E$.

Subsequently, in Figs. 5 through 8, the left, middle and right columns correspond to the positions $\boldsymbol{\xi}_4 = (0.375L_s, 0.5W_s)$, $\boldsymbol{\xi}_4 = (0.5L_s, 0.5W_s)$ (middle), and $\boldsymbol{\xi}_4 = (0.625L_s, 0.5W_s)$, respectively, of the thermocouple TC4. Figure 5 shows the estimated spatial temperature fields $\hat{T}(x, y, t) = \boldsymbol{\varphi}^{\mathrm{T}}(\mathbf{x})\hat{\boldsymbol{\theta}}_j$ of the specimen together with measurements of the four TCs of all three experiments. Measurements of TCi, $i = 1, 2, 3$ are indicated by $*$, while $\circ$ denotes the temperature recorded by TC4. The 2D normalized temperature fields are given in Figs. 5(Ai), $i = 1, 2, 3$ for the time $t = 1.5t_E$. Minor deviations between the temperature field and the setpoint temperature $T_{\mathrm{ref}}(t_E)$ occur close to the corners of the specimen fillet Ω_f. As explained in more detail by Jadachowski et al. (2016), this is mainly attributed to the geometry of the heating chamber (especially the vertical reflector) and the positioning of the vertical IR-lamps relative to the specimen and the reflector. In essence, the outer vertical IR-lamps transmit too much thermal radiation onto the center of the specimen and a uniform temperature profile along the direction y cannot be achieved.

Specific estimated temperature profiles along the directions x and y are plotted in Figs. 5(Bi) and Figs. 5(Ci), $i = 1, 2, 3$, respectively, for the times $t = 0.5t_E$ and $t = 1.5t_E$. Here, gray background areas indicate the specimen fillet. The spatial positions of the profiles were chosen

Post-print version of the article: L. Jadachowski, A. Steinboeck, and A. Kugi, "State estimation and advanced control of the 2D temperature field in an experimental oscillating annealing device", *Control Engineering Practice*, vol. 78, pp. 116–128, 2018, ISSN: 0967-0661. DOI: 10.1016/j.conengprac.2018.06.011

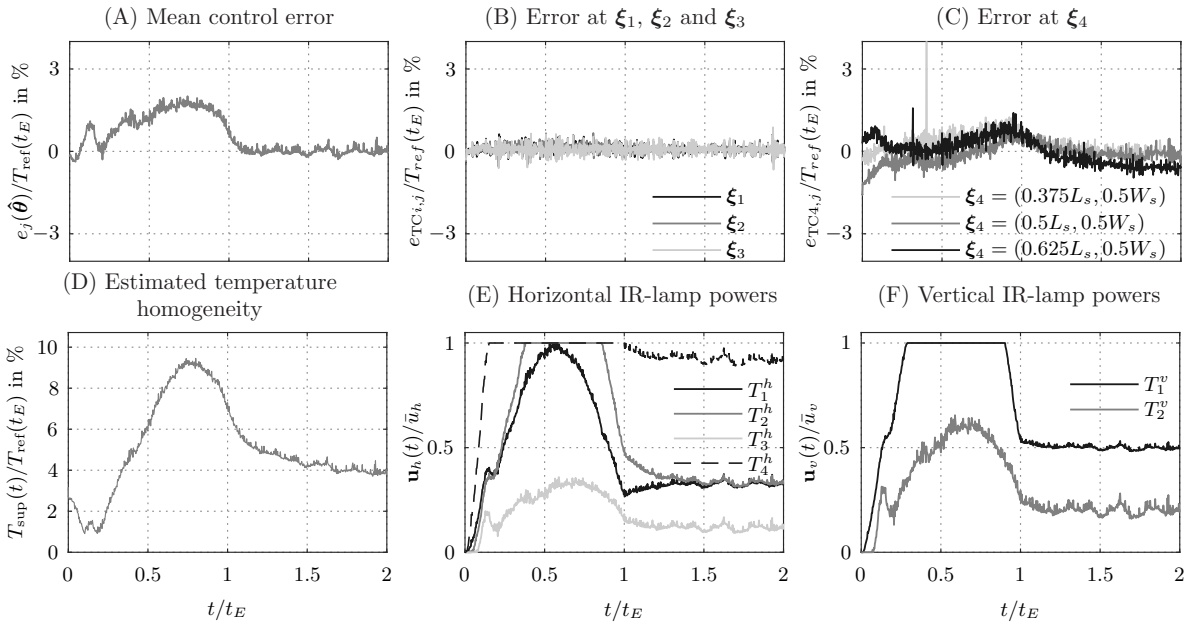

Figure 4: Measurement results of an annealing experiment with the non-oscillating specimen with the TC measurement $\Theta_4(t)$ located at $\boldsymbol{\xi}_4 = (0.5L_s, 0.5W_s)$: (A) the mean temperature tracking error; (B) the local observer errors $e_{\mathrm{TC}i,j}$, $i = 1,2,3$, at the positions $\boldsymbol{\xi}_1 = (0.25L_s, 0.5W_s)$, $\boldsymbol{\xi}_2 = (0.5L_s, 0.8W_s)$, $\boldsymbol{\xi}_3 = (0.75L_s, 0.5W_s)$; (C) the local observer error $e_{\mathrm{TC}4,j}$ at the position $\boldsymbol{\xi}_4$ for three experiments; (D) the estimated relative temperature homogeneity; (E) relative values of horizontal IR-lamps $\mathbf{u}_h(t)$; (F) relative values of vertical IR-lamps $\mathbf{u}_v(t)$.

to contain the positions of the TCs (cf. lines in Figs. 5(Ai), $i = 1,2,3$). Fig. 5 proves the good agreement between the TC measurements and the corresponding estimated temperatures. Two local spatial maxima of the estimated profiles occur along the x-coordinate at around $x = 0.375L_s$ and $x = 0.625L_s$. Also at these points the comparison with the TC4 measurements exhibits a very good accuracy of the observer. Only one spatial maximum is present along the direction y, where a more parabolic-like form of the temperature profiles can be observed.

All in all, the results shown in Figs. 4 and 5 confirm that the spatial temperature fields follow the reference temperature trajectory and that both the time evolution and the spatial distribution of the temperature fields are accurately estimated.

5.2. Experiments with an oscillating specimen

Separated temperature measurements for three experiments with the oscillating specimen position $\eta(t) = 3L_h \sin(2\pi t/\Pi)$, where $\Pi = 0.15t_E$ are presented in Fig. 6. In addition to the signals which are analogous to those given in Fig. 4, Fig. 6 shows also the measured oscillating position $\eta(t)$ of the specimen. In terms of the mean specimen temperature, the results presented in Figs. 6(Ai), $i = 1,2,3$ do not considerably deviate from the case with the fixed specimen position. In all three experiments, the relative mean control error reduces significantly for $t > t_E$ and is below 0.75 % of $T_{\mathrm{ref}}(t_E)$. In the transient heating phase, the mean error does not exceed 2 %. Again, the remaining control errors during the transient phase are mainly attributed to saturation of the IR-lamp powers. Time evolutions of the relative local estimation errors known by the EKF are plotted in Figs. 6(Bi), $i = 1,2,3$. Apart from some outliers in Fig. 6(B3), the signals $e_{\mathrm{TC}i,j}$, $i = 1,2,3$ are mainly below 0.5 % of $T_{\mathrm{ref}}(t_E)$. Figures 6(Ci), $i = 1,2,3$, show the time evolution of local estimation errors $e_{\mathrm{TC}4,j}$. The estimated local temperatures do not differ more than 3 % from the values measured by the thermocouple TC4. These results are not as accurate as those shown in Fig. 4(C) because the underlying EKF is based on the average model (11) which does not explicitly take into account the specimen oscillation. In Fig. 6(C1) and Fig. 6(C3), some oscillations that may correlate with the motion of the specimen are present. Such oscillations are absent in Fig. 6(C2). The reason for this behavior is that the TC positions $\boldsymbol{\xi}_4 = (0.375L_s, 0.5W_s)$ and $\boldsymbol{\xi}_4 = (0.625L_s, 0.5W_s)$ repeatedly pass by an active horizontal IR-lamp. This is not the case for the position $\boldsymbol{\xi}_4 = (0.5L_s, 0.5W_s)$. Moreover, from Fig. 4 and Fig. 6 it can be inferred that the assumption $\tau \gg \Pi$ (cf. Section 2.3) is only weakly satisfied for $\Pi = 0.15t_E$. It is expected that if $\Pi \ll 0.15t_E$, the temperature oscillations given in Fig. 6(C1) and Fig. 6(C3) will be negligibly small with a further reduction of the local estimation errors $e_{\mathrm{TC}i,j}$, $i = 1,\ldots,4$.

Post-print version of the article: L. Jadachowski, A. Steinboeck, and A. Kugi, "State estimation and advanced control of the 2D temperature field in an experimental oscillating annealing device", *Control Engineering Practice*, vol. 78, pp. 116–128, 2018, ISSN: 0967-0661. DOI: 10.1016/j.conengprac.2018.06.011

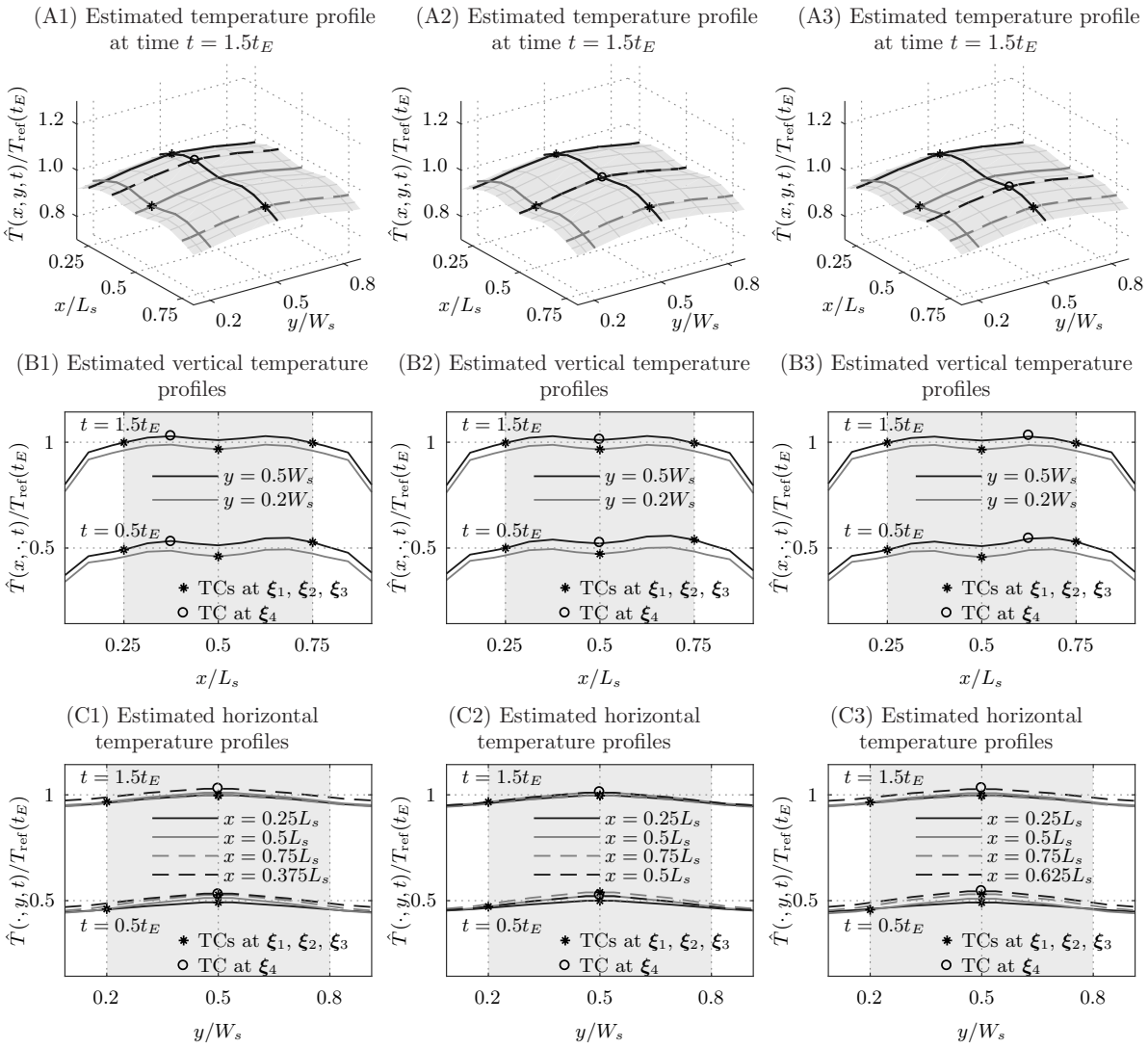

Figure 5: Estimated spatial temperature profiles of three annealing experiments with the fixed specimen position. The TC measurement $\Theta_4(t)$ located at three positions $\boldsymbol{\xi}_4 = (0.375L_s, 0.5W_s)$ (left), $\boldsymbol{\xi}_4 = (0.5L_s, 0.5W_s)$ (middle), and $\boldsymbol{\xi}_4 = (0.625L_s, 0.5W_s)$ (right). (A1), (A2), (A3): 2D relative temperature profiles of the specimen w.r.t. the target temperature at time $t = 1.5t_E$. (B1), (B2), (B3): comparison of relative temperature profiles $\hat{T}(x,\cdot,t)$ along the direction x through the TC positions $\boldsymbol{\xi}_i$, $i = 1,\ldots,4$ at the times $t = 0.5t_E$ and $t = 1.5t_E$. (C1), (C2), (C3): comparison of relative temperature profiles $\hat{T}(\cdot,y,t)$ along the direction y through the TC positions $\boldsymbol{\xi}_i$, $i = 1,\ldots,4$ at the times $t = 0.5t_E$ and $t = 1.5t_E$. Temperature measurements $\Theta_i(t)$ at the corresponding TC positions $\boldsymbol{\xi}_i$, $i = 1,\ldots,3$ ($*$) and at the position $\boldsymbol{\xi}_4$ ($\circ$). Gray background areas indicate the specimen fillet.

Figure 7 shows the corresponding time evolutions of the IR-lamp powers. In contrast to Fig. 4(E) and Fig. 4(F), in Fig. 7 only the horizontal IR-lamps saturate. The signals T_1^h and T_2^h are similar to those from Fig. 4(E) insofar as they converge to the same steady-state value. However, there are evident differences in the signals T_3^h and T_1^v. In case of the oscillating specimen, the vertical IR-lamps controlled by T_1^v do not saturate and emit, just as T_2^v, significantly less power than in case of the non-oscillating specimen. This is traded-off against the horizontal lamps controlled by T_3^h. They now emit as much as the lamps connected to T_4^h, they saturate in the transient heating phase, and they also arrive at the same steady-state value as T_4^h.

Estimated spatial temperature fields $\hat{T}(x,y,t) = \boldsymbol{\varphi}^{\mathrm{T}}(\mathbf{x})\hat{\boldsymbol{\theta}}_j$ and corresponding TC measurements are shown in Fig. 8 for the oscillating specimen. The 2D temperature profiles for the time $t = 1.5t_E$ are plotted in Figs. 8(Ai),

Post-print version of the article: L. Jadachowski, A. Steinboeck, and A. Kugi, "State estimation and advanced control of the 2D temperature field in an experimental oscillating annealing device", *Control Engineering Practice*, vol. 78, pp. 116–128, 2018, ISSN: 0967-0661. DOI: 10.1016/j.conengprac.2018.06.011

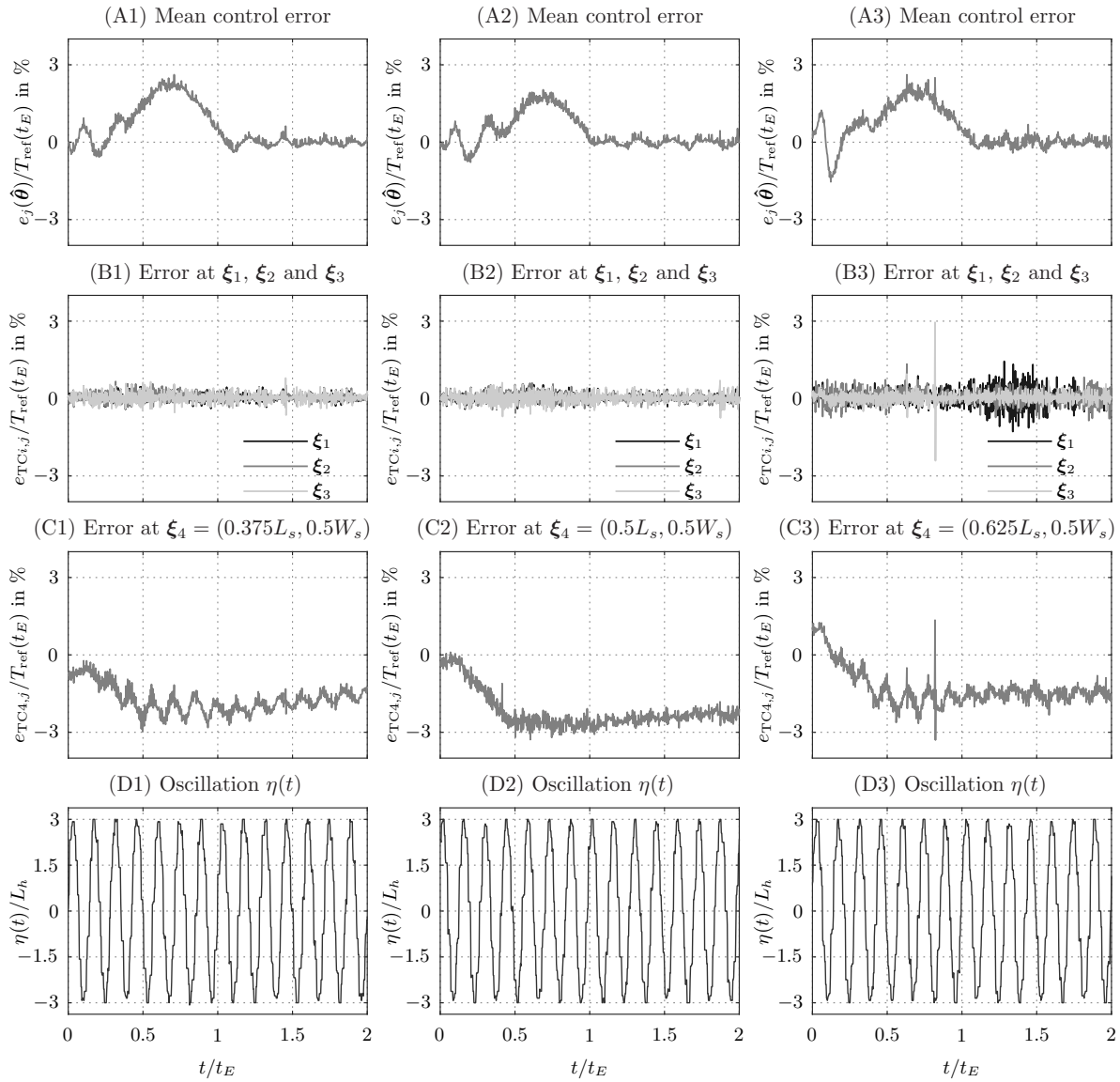

Figure 6: Measurement results of three annealing experiments with the oscillating specimen and the TC measurement $\Theta_4(t)$ located at three different positions $\boldsymbol{\xi}_4 = (0.375L_s, 0.5W_s)$ (left), $\boldsymbol{\xi}_4 = (0.5L_s, 0.5W_s)$ (middle), and $\boldsymbol{\xi}_4 = (0.625L_s, 0.5W_s)$ (right). Comparison of the mean temperature tracking errors, the local observer errors at the positions $\boldsymbol{\xi}_1 = (0.25L_s, 0.5W_s)$, $\boldsymbol{\xi}_2 = (0.5L_s, 0.8W_s)$, $\boldsymbol{\xi}_3 = (0.75L_s, 0.5W_s)$, the local temperature error at the position $\boldsymbol{\xi}_4$, and the position $\eta(t)$ of the oscillating specimen.

$i = 1, 2, 3$. Similar to the results from Fig. 5, minor deviations of the temperature field from the reference value $T_{\mathrm{ref}}(t_E)$ occur close to the corners of Ω_f. However, compared to Fig. 5, these deviations are now reduced due to the specimen motion and the adapted power distribution supplied to the IR-lamps. In fact, a comparison between Figs. 5(Bi) and Figs. 8(Bi), $i = 1, 2, 3$, reveals that the homogeneity of the vertical temperature profiles improved as a consequence of the specimen oscillation. Moreover, the temperature offset between the two evaluation lines along the direction x at $y = 0.2W_s$ and $y = 0.5W_s$ is reduced. The temperature profiles along the direction y passing through the TC positions $\boldsymbol{\xi}_i$, $i = 1, \ldots, 4$, are shown in Figs. 8(Ci), $i = 1, 2, 3$. While some minor inhomogeneities can be observed at different coordinates x at the time $t = 0.5t_E$, they are practically negligible for $t > t_E$.

To compare the temperature homogeneity in the fixed

Post-print version of the article: L. Jadachowski, A. Steinboeck, and A. Kugi, "State estimation and advanced control of the 2D temperature field in an experimental oscillating annealing device", *Control Engineering Practice*, vol. 78, pp. 116–128, 2018, ISSN: 0967-0661. DOI: 10.1016/j.conengprac.2018.06.011

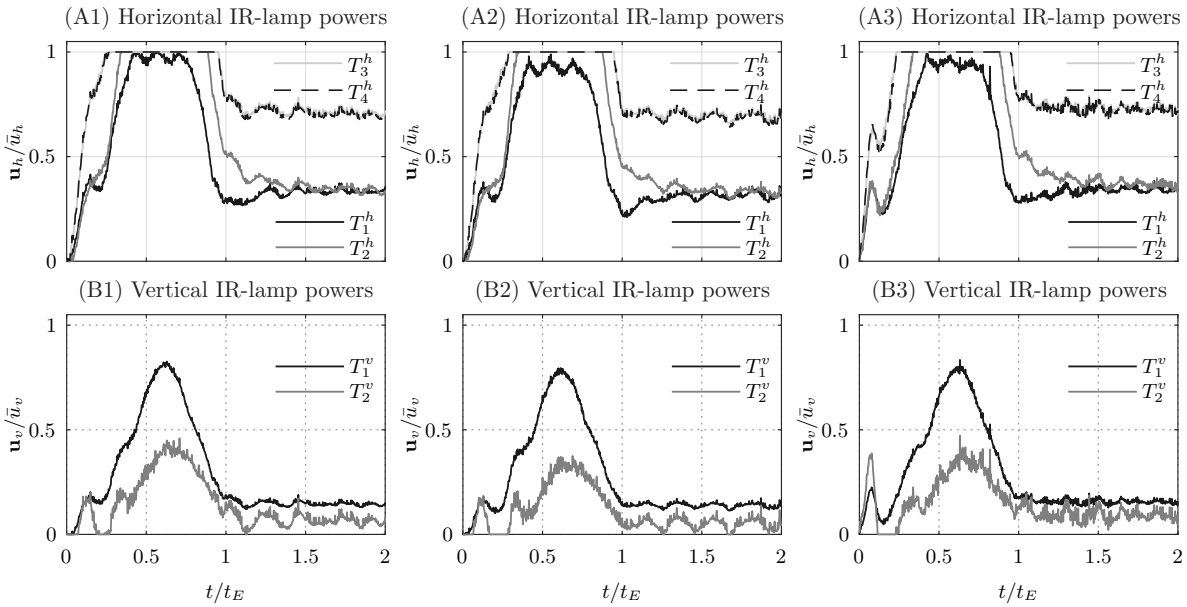

Figure 7: Measurement results of three annealing experiments with the oscillating specimen conducted with the TC measurement $\Theta_4(t)$ located at three different positions $\boldsymbol{\xi}_4 = (0.375L_s, 0.5W_s)$ (left), $\boldsymbol{\xi}_4 = (0.5L_s, 0.5W_s)$ (middle), and $\boldsymbol{\xi}_4 = (0.625L_s, 0.5W_s)$ (right). Comparison of the IR-lamp powers: relative values of horizontal IR-lamps $\mathbf{u}_h(t)$ (top) and vertical IR-lamps $\mathbf{u}_v(t)$ (bottom).

and the oscillating specimen, the normalized sup-norm $T_{\text{sup}}(t)$ is computed for all six experiments. Comparisons of $T_{\text{sup}}(t)$ between the oscillating and the non-oscillating specimen are shown in Fig. 9 for different positions $\boldsymbol{\xi}_4$ of the thermocouple TC4. Generally, the oscillation reduces the temperature non-uniformities. The increase of the temperature inhomogeneity for $t < t_E$ is attributed to the saturation of the control inputs in the transient heating phase. For $t > t_E$, when the mean temperature is already nearly constant (cf. Figs. 4(Ai) and Figs. 6(Ai), $i = 1, 2, 3$), the spatial temperature inhomogeneity continuously decreases. Its steady-state value is approximately 4 % of $T_{\text{ref}}(t_E)$ for the non-oscillating specimen and 2 % of $T_{\text{ref}}(t_E)$ for the oscillating specimen. This demonstrates again that the oscillation of the specimen significantly improves the control accuracy.

6. Conclusions

In this paper, an advanced control concept for an experimental annealing furnace with an oscillating steel specimen was developed and evaluated based on measurements. A distributed-parameter model of the 2D temperature evolution in the steel specimen was extended to take into account the oscillating motion of the specimen. In a first step, the Finite-Element (FE) method with a tailored non-equidistant discretization of the spatial domain was used to obtain a reduced-order model. In a second step, time averaging was applied to the FE-model. The resulting time-averaged FE model served as the basis for optimal feedforward trajectory planning, an EKF-based temperature estimation, and an LQG feedback control design.

The optimal feedforward control approach is based on a constant power distribution amplified by a time-dependent scalar factor. This approach allows a reasonable trade-off between computational costs and the control performance in terms of the temperature homogeneity. The spatial 2D temperature fields are estimated by means of the EKF. It uses only three thermocouples for local temperature measurements of the specimen surface. A fourth existing thermocouple measurement was used to validate the estimation performance. The LQG feedback tracking controller is used to minimize errors between the desired and the estimated temperature profiles. The controller was augmented by an integral term to eliminate the mean steady-state control error of the specimen temperature.

Experiments with both the fixed and the oscillating specimen were conducted. In both cases, practically the same good tracking accuracy in terms of the mean temperature was achieved. A very good estimation performance is achieved when the specimen does not move. This is mainly attributed to the accuracy of the mathematical model for the fixed specimen position. Here, the resulting temperature inhomogeneity does not exceed 10 % of the setpoint temperature during the transient heating phase and reduces to less than 4 % in the steady state. The systematic consideration of a periodic specimen oscillation in all design steps results in a significant reduction of the spatial temperature inhomogeneity and a good overall estimation and tracking accuracy. In essence, the temperature

Post-print version of the article: L. Jadachowski, A. Steinboeck, and A. Kugi, "State estimation and advanced control of the 2D temperature field in an experimental oscillating annealing device", *Control Engineering Practice*, vol. 78, pp. 116–128, 2018, ISSN: 0967-0661. DOI: 10.1016/j.conengprac.2018.06.011

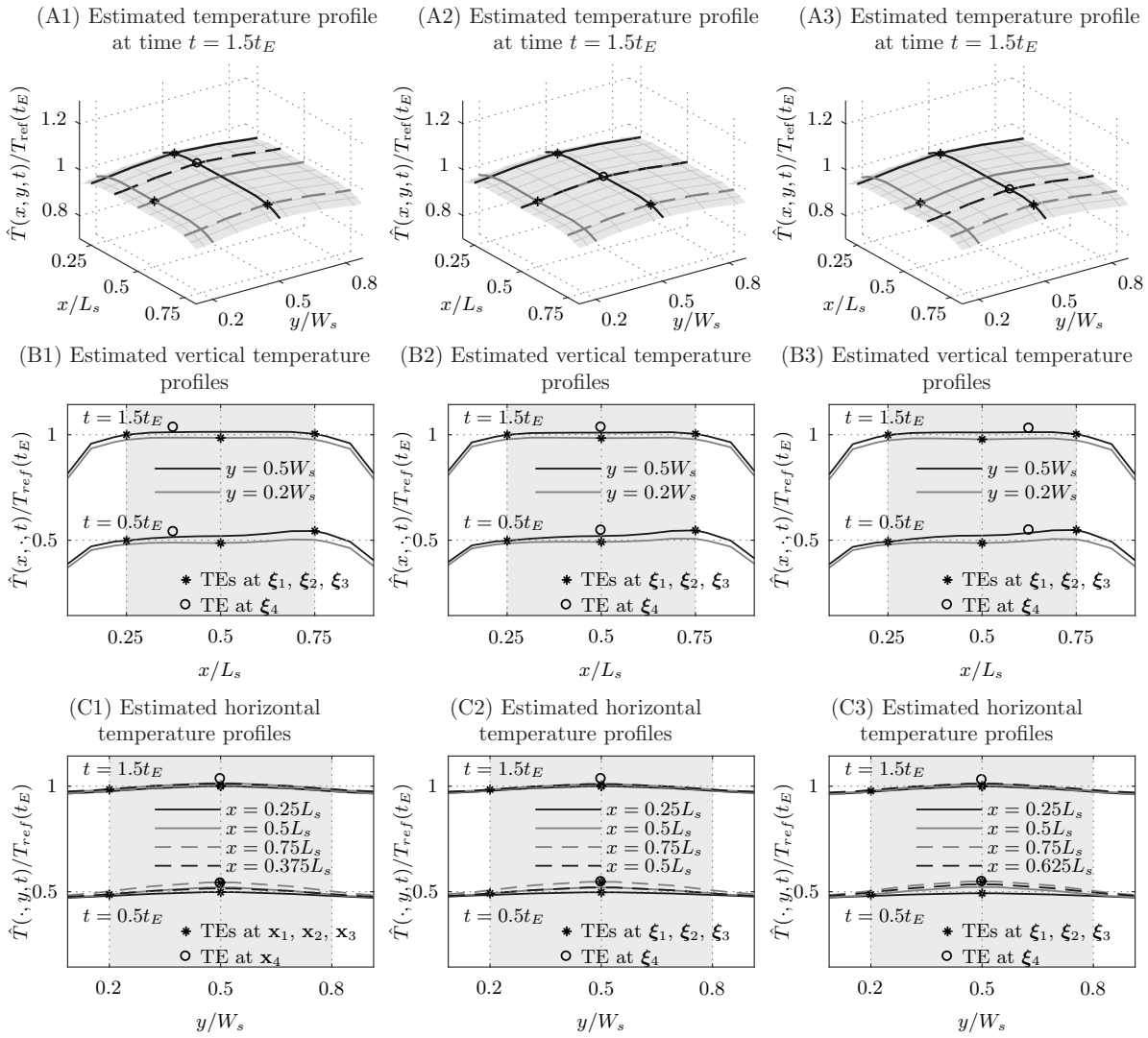

Figure 8: Calculated spatial temperature profiles of three annealing experiments with the oscillating specimen. The TC measurement $\Theta_4(t)$ located at three positions: $\boldsymbol{\xi}_4 = (0.375L_s, 0.5W_s)$ (left), $\boldsymbol{\xi}_4 = (0.5L_s, 0.5W_s)$ (middle), and $\boldsymbol{\xi}_4 = (0.625L_s, 0.5W_s)$ (right). (A1), (A2), (A3): 2D relative temperature profiles of the specimen w.r.t. the target temperature at time $t = 1.5t_E$. (B1), (B2), (B3): comparison of relative temperature profiles $\hat{T}(x, \cdot, t)$ along the direction x through the TC positions $\boldsymbol{\xi}_i$, $i = 1, \ldots, 4$ at the times $t = 0.5t_E$ and $t = 1.5t_E$. (C1), (C2), (C3): comparison of relative temperature profiles $\hat{T}(\cdot, y, t)$ along the direction y through the TC positions $\boldsymbol{\xi}_i$, $i = 1, \ldots, 4$ at the times $t = 0.5t_E$ and $t = 1.5t_E$. Temperature measurements $\Theta_i(t)$ at the corresponding TC positions $\boldsymbol{\xi}_i$, $i = 1, \ldots, 3$ ($*$) and at the position $\boldsymbol{\xi}_4$ ($\circ$). Gray background areas indicates the specimen fillet.

inhomogeneity under steady-state operating conditions is halved by an oscillating specimen motion compared to a non-oscillating specimen.

Acknowledgement

The financial support by the Austrian Federal Ministry for Digital, Business and Enterprise, and the National Foundation for Research, Technology and Development, and voestalpine Stahl GmbH is gratefully acknowledged.

References

Abeykoon, C., Li, K., McAfee, M., Martin, P.J., Niu, Q., Kelly, A.L., and Deng, J. (2011). A new model based approach for the prediction and optimisation of thermal homogeneity in single screw extrusion. *Control Engineering Practice*, 19(8), 862–874.

Antoulas, A. (2005). *Approximation of Large-scale Dynamical Systems*. Advances in Design and Control. Society for Industrial and Applied Mathematics, Philadelphia, USA, 6th edition.

Böhm, T. and Meurer, T. (2017). Trajectory planning and tracking control for the temperature distribution in a deep drawing tool. *Control Engineering Practice*, 64, 127–139.

Post-print version of the article: L. Jadachowski, A. Steinboeck, and A. Kugi, "State estimation and advanced control of the 2D temperature field in an experimental oscillating annealing device", *Control Engineering Practice*, vol. 78, pp. 116–128, 2018, ISSN: 0967-0661. DOI: 10.1016/j.conengprac.2018.06.011

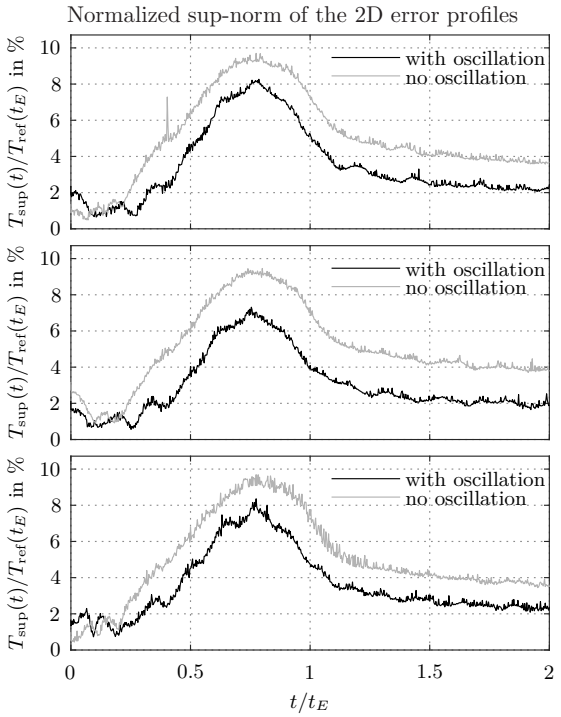

Figure 9: Estimated relative temperature homogeneity of the specimen during annealing experiments with and without specimen oscillation: $\Theta_4(t)$ located at $\boldsymbol{\xi}_4 = (0.375L_s, 0.5W_s)$ (top), $\Theta_4(t)$ located at $\boldsymbol{\xi}_4 = (0.5L_s, 0.5W_s)$ (middle), and $\Theta_4(t)$ located at $\boldsymbol{\xi}_4 = (0.625L_s, 0.5W_s)$ (bottom).

Bordignon, L., Angeli, G., Bolt, H., Hekkens, R., Maschek, W., Paavilainen, J., and Eynde, X. (2002). Enhanced hot dip galvanising by controlled oxidation in the annealing furnace. *Proceedings of the 44th Mechanical Working and Steel Processing Conference (MWSP), Orlando, USA, 8–11 Sep. 2002*, Vol. XL, 833–844.

Cohen, M.F. and Greenberg, D.P. (1985). The Hemi-Cube: A Radiosity Solution for Complex Environments. *Computer Graphics*, 19(3), 31–40.

Ebert, J., de Roover, D., Porter, L., Lisiewicz, V., Ghosal, S., Kosut, R., and Emami-Naeini, A. (2004). Model-based control of rapid thermal processing for semiconductor wafers. In *Proceedings of the 2004 American Control Conference, Boston, USA, 30 Jun.–2 Jul. 2004*, volume 5, 3910–3921.

Franklin, G., Powell, J., and Workman, M. (1997). *Digital Control of Dynamic Systems*. Prentice Hall, Upper Saddle River, NJ, 3rd edition.

Girault, M. and Videcoq, E. (2013). Temperature regulation and tracking in a MIMO system with a mobile heat source by LQG control with a low order model. *Control Engineering Practice*, 21(3), 333–349.

Hippe, P. (2006). *Windup in Control: Its Effects and Their Prevention*. Advances in Industrial Control. Springer, London.

Incropera, F.P., Dewitt, D.P., Bergman, T.L., and Lavine, A.S. (2007). *Fundamentals of Heat and Mass Transfer*. John Wiley & Sons, Hoboken, New Jersey, 6th edition.

Jadachowski, L., Steinboeck, A., and Kugi, A. (2016). Optimal steady-state temperature field in an experimental annealing furnace. *IFAC-PapersOnLine*, 49(20), 214–219. 17th IFAC Symposium on Control, Optimization and Automation in Mining, Mineral and Metal Processing – Vienna, Austria, 31 Aug.–2 Sep. 2016.

Jadachowski, L., Steinboeck, A., and Kugi, A. (2017a). Feedforward control of the temperature field in an experimental annealing furnace. *IFAC-PapersOnLine*, 50(1), 13790–13795. 20th IFAC World Congress – Toulouse, France, 9–14 Jul. 2017.

Jadachowski, L., Steinboeck, A., and Kugi, A. (2017b). Two-dimensional thermal modeling with specular reflections in an experimental annealing furnace. *Mathematical and Computer Modelling of Dynamical Systems*, 23(1), 23–39.

Jadachowski, L., Steinboeck, A., and Kugi, A. (2018). Model Averaging and Feedforward Control in an Oscillating Annealing Furnace. *IFAC-PapersOnLine*. Submitted to the 5th IFAC Workshop on Mining, Mineral and Metal Processing – Shanghai, China, 23–25 Aug. 2018.

Khalil, H. (2002). *Nonlinear Systems*. Pearson Education. Prentice Hall, Upper Saddle River, USA, 3rd edition.

Lipár, S., Noga, P., and Hulkó, G. (2013). Modelling and Control of Extruder Barrel Temperature Field. *IFAC Proceedings Volumes*, 46(26), 191–196. 1st IFAC Workshop on Control of Systems Governed by Partial Differential Equations, France, Paris, 25–27 Sep. 2013.

Logerais, P.O., Riou, O., Delaleux, F., Durastanti, J.F., and Bouteville, A. (2015). Improvement of temperature homogeneity of a silicon wafer heated in a rapid thermal system (RTP: Rapid Thermal Process) by a filtering window. *Applied Thermal Engineering*, 77, 76–89.

Matthies, K. (2001). Time-Averaging under Fast Periodic Forcing of Parabolic Partial Differential Equations: Exponential Estimates. *Journal of Differential Equations*, 174(1), 133–180.

Modest, M. (2003). *Radiative Heat Transfer*. Academic Press, Burlington, 2nd edition.

Mullinger, P. and Jenkins, B. (2014). *Industrial and Process Furnaces: Principles, Design and Operation*. Butterworth-Heinemann, Amsterdam, 2 edition.

Niederer, M., Strommer, S., Steinboeck, A., and Kugi, A. (2016). Nonlinear model predictive control of the strip temperature in an annealing furnace. *Journal of Process Control*, 48, 1–13.

Reddy, J. and Gartling, D. (2010). *The Finite Element Method in Heat Transfer and Fluid Dynamics*. Computational Mechanics and Applied Analysis. CRC Press, Boca Raton, 3rd edition.

Rötzer, F., Jadachowski, L., and Kugi, A. (2017). Model reduction, observer design and sensor placement for an infrared annealing furnace. *at - Automatisierungstechnik*, 65(5), 337–349. [in German].

Seyrkammer, H., Almer, D., Fuchshumer, S., Rieger, K., Schöberl, M., and Schlacher, K. (2010). Flatness-based temperature control of metal sheets. *IFAC Proceedings Volumes*, 43(18), 8–15. 5th IFAC Symposium on Mechatronic Systems, USA, Cambridge, 13–15 Sep. 2010.

Shen, L., He, J., Yang, C., Gui, W., and Xu, H. (2016). Temperature Uniformity Control of Large-Scale Vertical Quench Furnaces for Aluminum Alloy Thermal Treatment. *IEEE Transactions on Control Systems Technology*, 24(1), 24–39.

Siegel, R. and Howell, J. (2002). *Thermal Radiation Heat Transfer*. Taylor & Francis, New York, 4th edition.

Simon, D. (2006). *Optimal State Estimation: Kalman, H_∞, and Nonlinear Approaches*. John Wiley & Sons, New Jersey.

Strommer, S., Niederer, M., Steinboeck, A., and Kugi, A. (2018). Hierarchical nonlinear optimization-based controller of a continuous strip annealing furnace. *Control Engineering Practice*, 73, 40–55.

Totten, G. (2006). *Steel Heat Treatment: Metallurgy and Technologies*. Taylor & Francis, Boca Raton, 2nd edition.

Vande Wouwer, A., Point, N., Porteman, S., and Remy, M. (2000). An approach to the selection of optimal sensor locations in distributed parameter systems. *Journal of Process Control*, 10(4), 291–300.

Wächter, A. and Biegler, L.T. (2006). On the implementation of an interior-point filter line-search algorithm for large-scale nonlinear programming. *Mathematical Programming*, 106(1), 25–57.

Post-print version of the article: L. Jadachowski, A. Steinboeck, and A. Kugi, "State estimation and advanced control of the 2D temperature field in an experimental oscillating annealing device", *Control Engineering Practice*, vol. 78, pp. 116–128, 2018, ISSN: 0967-0661. DOI: 10.1016/j.conengprac.2018.06.011